Provided for non-commercial research and education use.
Not for reproduction, distribution or commercial use.

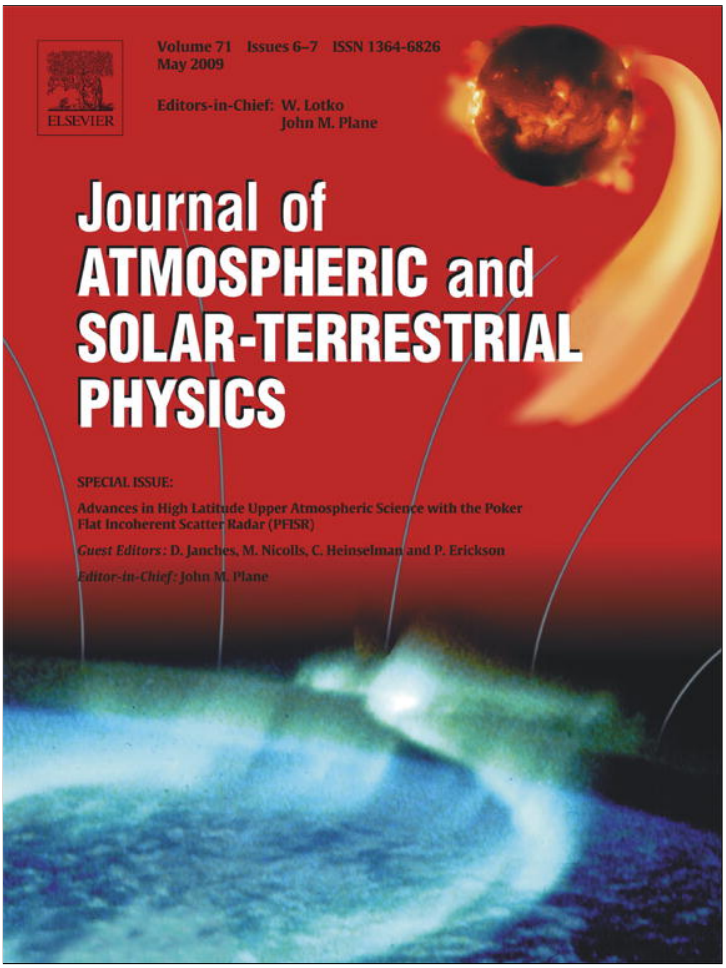

This article appeared in a journal published by Elsevier. The attached copy is furnished to the author for internal non-commercial research and education use, including for instruction at the authors institution and sharing with colleagues.

Other uses, including reproduction and distribution, or selling or licensing copies, or posting to personal, institutional or third party websites are prohibited.

In most cases authors are permitted to post their version of the article (e.g. in Word or Tex form) to their personal website or institutional repository. Authors requiring further information regarding Elsevier's archiving and manuscript policies are encouraged to visit:

http://www.elsevier.com/copyright

Author's personal copy

Journal of Atmospheric and Solar-Terrestrial Physics 71 (2009) 744–770

Contents lists available at ScienceDirect

Journal of
Atmospheric and Solar-Terrestrial Physics

journal homepage: www.elsevier.com/locate/jastp

Temporal evolution of neutral, thermospheric winds and plasma response using PFISR measurements of gravity waves

Sharon L. Vadas [a,*], Michael J. Nicolls [b]

[a] NorthWest Research Associates, CoRA Div., 3380 Mitchell Lane, Boulder, CO 80503, USA
[b] Center for Geospace Studies, SRI International, 333 Ravenswood Ave., Menlo Park, CA 94025, USA

ARTICLE INFO

Article history:
Accepted 7 January 2009
Available online 3 March 2009

Keywords:
Gravity waves
Neutral dynamics
Modeling
Thermosphere
Ionosphere

ABSTRACT

In this paper, we analyze the temporal variability of the propagation and dissipation of two southeast (SE)ward-propagating gravity waves (GWs) observed by the Poker Flat Incoherent Scatter Radar (PFISR) on 13 December 2006. We determine the GW vertical wavelengths as a function of altitude along each constant wave phase line, then extract the neutral, horizontal winds every ~10–12 min (one-half of a wave period) along the direction of GW propagation as a function of altitude using an accurate, dissipative GW dispersion relation and MSIS temperatures. We find that the neutral wind in the northwest (NW) direction above PFISR was composed of a slowly varying "mean" of ~ -150 m/s plus a slowly moving, large-scale wave with a period of 3–5 h. These winds added at $z\sim190$ km, creating a large NW wind of $\sim -(200-250)$ m/s. This wind caused these two GWs to become evanescent or nearly evanescent some of the time, although their amplitudes increased up to $z\sim210-240$ km. We find that the winds accelerated in the SEward direction by ~100–150 m/s in 30–40 min at $z\sim190$ km. We hypothesize that these accelerations are thermospheric body forces caused by the dissipation of SEward-propagating GWs excited by mountain wave breaking near the mesopause NW of PFISR. This hypothesis is supported by tropospheric winds and the consistency of the observed GW periods. Finally, we ray trace these GWs through the extracted winds, and using a simple single-ion plasma model, compare the theoretical and measured plasma responses. We find that theory agrees reasonably well with observations.

© 2009 Elsevier Ltd. All rights reserved.

1. Introduction

As a gravity wave (GW) propagates upwards in the thermosphere, its amplitude grows rapidly until it reaches its dissipation altitude, whereupon its amplitude decays rapidly with altitude and time. Although a GW's horizontal wavelength, λ_H, remains constant with altitude if the winds and temperatures change only with altitude, its vertical wavelength λ_z changes with altitude as a result of changing winds, temperatures, and dissipation due to kinematic viscosity and thermal diffusivity (e.g., Hines, 1960; Pitteway and Hines, 1963; Richmond, 1978). This refraction is observed as changes in the slopes of a GW's lines of constant phase with altitude and time, since a GW's phase is proportional to $\exp(i\int(m\,dz-\omega_r\,dt))$, where $m=2\pi/\lambda_z$ is the vertical wavenumber and ω_r is the observed wave frequency.

Until recently, GW propagation in the thermosphere with dissipation was mainly accomplished with multi-layer techniques (Midgley and Liemohn, 1966; Volland, 1969; Klostermeyer, 1972; Hickey and Cole, 1988), numerical simulations (Richmond, 1978; Francis, 1973; Zhang and Yi, 2002), and approximate or numerical solutions to complex dispersion relations (Pitteway and Hines, 1963; Yeh et al., 1975; Hickey and Cole, 1987). Recently, a more complete and accurate, analytic expression was derived for the amplitude decay and dispersion of a GW (Vadas and Fritts, 2005, hereafter VF2005). This description includes kinematic viscosity and thermal diffusivity, but neglects ion drag and wave-induced diffusion. Ion drag is unimportant during the night for GWs with periods less than a few hours and for GWs with periods less than an hour during the day (Hines and Hooke, 1970; Francis, 1973; Hocke and Schlegel, 1996; Gossard and Hooke, 1975). For $\lambda_H\approx200-400$ km, wave-induced diffusion significantly affects those GWs with periods longer than an hour (DelGenio and Schubert, 1979). Since GWs that reach $z\sim200$ km from the lower atmosphere under varying winds have periods less than an hour (Fritts and Vadas, 2008), neglecting ion drag and wave-induced diffusion is a good approximation for these waves.

The understanding of the propagation and dissipation of a GW in the thermosphere requires an accurate dissipative GW dispersion relation, λ_H, and the GW's observed period τ_r, as well as

* Corresponding author. Tel.: +1 303 4159701x202; fax: +1 303 4159702.
E-mail addresses: vasha@cora.nwra.com (S.L. Vadas), michael.nicolls@sri.com (M.J. Nicolls).

1364-6826/$ - see front matter © 2009 Elsevier Ltd. All rights reserved.
doi:10.1016/j.jastp.2009.01.011

Author's personal copy

the background neutral winds and temperatures. Conversely, if λ_H, τ_r, and $\lambda_z(z)$ are known instead along with the background temperatures, then the average, background, horizontal neutral wind along the GW propagation direction can be calculated using a GW dissipative dispersion relation. Observations of GWs with the Poker Flat Incoherent Scatter Radar (PFISR), which are observed as traveling ionospheric disturbances, or TIDs, have the capability of providing λ_H, τ_r, and $\lambda_z(z)$.

A recent PFISR experiment that included 10 essentially simultaneous look directions observed a southeast (SE)ward-propagating GW on 13 December 2006 from 2200–2400 UT (Nicolls and Heinselman, 2007). Using a temporally averaged $\lambda_z(z)$ profile that neglected corrections due to range-smearing and other effects, and the GW dissipative dispersion relation derived in VF2005, Vadas and Nicolls (2008) calculated this GW's intrinsic frequency profile, $\omega_{Ir}(z)$, which varied with altitude primarily because of Doppler-shifting from vertically varying background, neutral winds in the thermosphere. They then extracted the average, neutral, background, horizontal winds from $z\sim170-250$ km along the GW propagation direction using MSIS temperatures. They also used the mean component of the anti-parallel ion velocity, V_{los}, to calculate the neutral wind along the magnetic meridian, although this calculation was somewhat uncertain because diffusion was neglected and errors on the velocity measurements were quite large. They found that although the neutral winds at $z\sim170$ km and $z\geqslant220$ km were consistent with tides, with $U_H\sim-150$ m/s, the winds at $z\sim180-190$ km were much larger, with $U_H\sim-250$ m/s. This sharp increase and decrease in the neutral winds occurred over a vertical depth of only $\sim$40 km, and were unlikely due to tides because tidal amplitudes are viscously limited above $z\sim150$ km (e.g., Roble, 1995). However, the temporal evolution of this strong, thermospheric wind was not calculated; thus, the underlying temporal evolution of this neutral wind was not studied.

The purpose of this paper is to calculate the temporal evolution, acceleration, and individual components of the thermospheric, neutral, horizontal wind over a 4-h period on 13 December at altitudes of $z\sim180-250$ km using GW dissipative theory and PFISR TID-measurements with range-smearing corrections, and to estimate a possible source of these observed GWs. We will also compare the measured plasma response with that estimated from a simple plasma model and ray tracing. We analyze the temporal evolution using the same GW measured by PFISR as discussed in Nicolls and Heinselman (2007) and Vadas and Nicolls (2008), but extend the analysis backwards in time by 2 h to include a second GW propagating in nearly the same direction. In Section 2, we briefly review the dissipative GW dispersion relation and amplitude decay expressions we use here. Section 3 provides details of the PFISR observations for the GWs we analyze here and review the process by which we extract GW vertical wavelengths from the lines of constant phase measured in different look directions. In Section 4, we use the PFISR measurements and GW dissipative theory to calculate the temporally and spatially varying background neutral winds and wind accelerations that these GWs propagated through in the thermosphere. We also investigate the slowly varying mean wind and a large-scale, slowly moving wave, both of which are components of the extracted neutral winds. Section 5 shows the horizontal and vertical velocity perturbation profiles as a function of altitude for these GWs determined via ray tracing these GWs through the calculated, background, neutral winds. We also calculate the plasma response to these GWs using a simple, single-species ion model, and compare with the observed response. Section 6 provides a hypothesis for a possible source of these GWs and of the calculated thermospheric accelerations.

2. GW dissipative theory

VF2005 derived an analytic expression for the GW anelastic dispersion relation of a high-frequency, dissipating GW in the thermosphere by postulating that the GW solution (after scaling the mean density $\overline{\rho}$ out of the fluid variables appropriately) from a temporally localized source can be written as decaying explicitly in time and implicitly in altitude. This is equivalent to setting the wave frequency, rather than $m=2\pi/\lambda_z$ (as in all previous derivations, e.g., Pitteway and Hines, 1963) to be complex. Unlike the inseparable complex equation one obtains if m is assumed complex, this approach yields a complex dispersion relation which is analytically separable into a real GW dispersion relation and a real expression for the GW amplitude's decay in time.

This dispersion relation includes the dissipative effects of kinematic viscosity and thermal diffusivity, and assumes that ion drag and wave-induced diffusion can be neglected, which is a good assumption for GWs with periods less than an hour during the daytime. Unlike previous solutions which were not valid for strong dissipation because they were derived from perturbation expansions in kinematic viscosity (e.g., Pitteway and Hines, 1963), this solution is accurate during strong dissipation, and is exact for a high-frequency GW with a phase speed much less than the speed of sound and which propagates through an atmosphere with constant temperature, wind, kinematic viscosity, and Prandtl number. In order for the kinematic viscosity to be considered locally constant, this GW must have $\lambda_z\ll4\pi$H during strong dissipation, where H is the neutral density scale height. This dispersion relation is (VF2005)

$$m^2=\frac{k_H^2N^2}{\omega_{Ir}^2(1+\delta_++\delta^2/Pr)}\left[1+\frac{\nu^2}{4\omega_{Ir}^2}\left(\mathbf{k}^2-\frac{1}{4\mathrm{H}^2}\right)^2\times\frac{(1-Pr^{-1})^2}{(1+\delta_+/2)^2}\right]^{-1}-k_H^2-\frac{1}{4\mathrm{H}^2},\tag{1}$$

where $\mathbf{k}=(k,l,m)$ is the GW zonal, meridional, and vertical wavenumber components in geographic coordinates, respectively, $(\lambda_x=2\pi/k,\ \lambda_y=2\pi/l,\ \lambda_z=2\pi/m)$ is the wavelength vector, $k_H^2=k^2+l^2$, $\mathbf{k}^2=k_H^2+m^2$, N is the buoyancy frequency, Pr is the Prandtl number, μ is the viscosity coefficient, $\nu=\mu/\overline{\rho}$ is the kinematic viscosity, $\overline{\rho}$ is the mean density, $\mathrm{H}=-\overline{\rho}(d\overline{\rho}/dz)^{-1}$ is the density scale height, $\delta=\nu m/\mathrm{H}\omega_{Ir}$, and $\delta_+=\delta(1+Pr^{-1})$. Additionally, the intrinsic frequency is $\omega_{Ir}=\omega_r-kU-lV$, which can be rewritten as

$$\omega_{Ir}=\omega_r-k_HU_H,\tag{2}$$

where $\omega_r=2\pi/\tau_r$ is the constant, ground-based or observed frequency, $U_H=(kU+lV)/k_H$ is the background, neutral wind along the direction of GW propagation, and U and V are the zonal and meridional neutral wind components, respectively, in geographic coordinates.

Additionally, assuming negligible wave reflection from viscosity, which can cause a GW to partially reflect downwards as it continues to propagate upwards (Midgley and Liemohn, 1966; Yanowitch, 1967; Volland, 1969), a GW's amplitude grows in altitude as $\propto1/\sqrt{\overline{\rho}}$, but decays from dissipation as $\exp(\omega_{Ii}t)$, where ω_{Ii} is the dissipative decay rate (VF2005):

$$\omega_{Ii}=-\frac{\nu}{2}\left(\mathbf{k}^2-\frac{1}{4\mathrm{H}^2}\right)\frac{[1+(1+2\delta)/Pr]}{(1+\delta_+/2)}.\tag{3}$$

The ray-trace code which utilizes these expressions is described in detail in Vadas (2007). It is important to note that although $\lambda_z(z)$ (or $U_H(z)$) can be determined from Eq. (1), ray tracing is necessary to determine a GW's amplitude as a function of altitude and/or time via Eq. (3).

Author's personal copy

The vertical group velocity of a dissipating GW is (Eq. (C3) from VF2005)

$$c_{g_z} = \frac{1}{\omega_{Ir}\mathscr{B}}\left\{ m\left[-\frac{k_H^2 N^2}{(\mathbf{k}^2 + 1/4\mathrm{H}^2)^2} - \frac{v^2}{2}(1-Pr^{-1})^2\left(\mathbf{k}^2 - \frac{1}{4\mathrm{H}^2}\right)\frac{(1+\delta_+ + \delta^2/Pr)}{(1+\delta_+/2)^2} + \frac{v^4(1-Pr^{-1})^4}{16\mathrm{H}^2\omega_{Ir}^2}\frac{(\mathbf{k}^2 - 1/4\mathrm{H}^2)^2}{(1+\delta_+/2)^3} - \frac{v^2}{Pr\mathrm{H}^2}\right] - \frac{v_+\omega_{Ir}}{2\mathrm{H}}\right\}, \quad (4)$$

where $v_+ = v(1+Pr^{-1})$ and

$$\mathscr{B} = \left[1 + \frac{\delta_+}{2} + \frac{\delta^2 v^2}{16\omega_{Ir}^2}(1-Pr^{-1})^4\frac{(\mathbf{k}^2 - 1/4\mathrm{H}^2)^2}{(1+\delta_+/2)^3}\right]. \quad (5)$$

When dissipation is negligible, $\delta \sim v \sim 0$. In this case, the GW dispersion relation, Eq. (1), reduces to the well-known expression

$$m^2 = \frac{k_H^2 N^2}{\omega_{Ir}^2} - k_H^2 - \frac{1}{4\mathrm{H}^2}, \quad (6)$$

and the vertical group velocity, Eq. (4), reduces to

$$c_{g_z} \simeq -\frac{1}{\omega_{Ir}}\frac{m k_H^2 N^2}{(\mathbf{k}^2 + 1/4\mathrm{H}^2)^2}. \quad (7)$$

In this case, $m<0$ ($m>0$) denotes an upward-propagating (downward-propagating) GW, since $c_{g_z}>0$ ($c_{g_z}<0$). However, when a GW is strongly dissipating, $m<0$ may denote either a downward or an upward-propagating GW from Eq. (4), as we will see for a specific GW in a moment.

An important assumption used to derive these GW dissipative expressions is that the background wind shears are not too large (Vadas and Fritts, 2006, hereafter VF2006):

$$|\lambda_z| < 2\pi |U_H/(dU_H/dz)|. \quad (8)$$

A typical F region GW with $\lambda_z \simeq 100-300$ km (e.g., Djuth et al., 1997) will refract according to Eq. (8) if $dU_H/dz < U_H(0.02-0.06)$ m/s/km, which is a wind shear of $dU_H/dz < (4-12)$ m/s/km for a background wind of $U_H \simeq 200$ m/s. A GW's λ_z may only reflect the actual wind if Eq. (8) is satisfied everywhere in the thermosphere; otherwise, λ_z may instead reflect the average, neutral wind. Because of strong viscous damping, however, large neutral vertical wind shears cannot be maintained for a long time in the thermosphere; neutral horizontal winds in excess of tidal winds dissipate rapidly, within 60 min at $z \sim 190$ km (see Section 6.3).

Finally, a GW's dissipation altitude can be estimated via the quenching criterion (VF2006):

$$v_{\mathrm{diss}} \simeq \frac{|k_H m| N}{2\mathrm{H}(\mathbf{k}^2 + 1/4\mathrm{H}^2)^{5/2}}. \quad (9)$$

Eq. (9) is solved iteratively for $m_a = |2\pi/\lambda_z|$ as

$$m_a = \sqrt{\left(\frac{k_H N}{2\mathrm{H}v}\right)^{2/5} m_a^{2/5} - k_H^2 - \frac{1}{4\mathrm{H}^2}}, \quad (10)$$

where the first guess for m_a on the right-hand-side (RHS) of Eq. (10) is

$$m_a = \sqrt{\sqrt{\frac{k_H N}{2\mathrm{H}v}} - k_H^2 - \frac{1}{4\mathrm{H}^2}}, \quad (11)$$

and the second guess for m_a on the RHS of Eq. (10) is the value of m_a determined on the left-hand side of Eq. (10) from the first iteration. This procedure is iterated until convergence in m_a is obtained.

Fig. 1 shows the vertical wavelength as a function of altitude for a high-frequency GW with $\lambda_H = 217$ km and $\tau_r = 20.2$ min, propagating through zero background winds $U = V = 0$. This figure was obtained by calculating the left- and right-hand sides of the dispersion relation, Eq. (1), for 200,000 equally spaced values of $\lambda_z = [-1000, 1000]$ km every 2 km vertically from $z = 150$ to 350 km. If the left- and right-hand sides were within 0.1% for a GW with vertical wavelength λ_z at altitude z, it is plotted in Fig. 1 as a dot. In the lower thermosphere where dissipation is negligible, upward (downward)-propagating GWs have negative (positive) m, as discussed previously. The left-hand side of this figure (with negative m) indicates the vertical wavelength that this upward-propagating GW has from $z \sim 150$ to 260 km. At $z \sim 260$ km, this upward-propagating GW reflects downwards because $c_{g_z} < 0$, although m remains negative after reflection. This is because the GW is virtually completely dissipated when it reflects, having strongly dissipated at a much lower altitude; therefore, its vertical group velocity cannot be approximated by Eq. (7). In fact, when the neutral winds are zero, this GW's momentum flux is maximum at the "dissipation altitude" of $z_{\mathrm{diss}} \sim 165$ km as determined via ray tracing (see Fig. 2 of Vadas and Nicolls, 2008). Although Fig. 1 is useful for understanding how this GW's vertical wavelength varies with altitude as it propagates and dissipates, it does not show at what altitude this GW dissipates, nor how its amplitude varies with altitude, because the dispersion relation contains no amplitude information. Instead, we must ray trace this GW in order to determine its amplitude via Eq. (3).

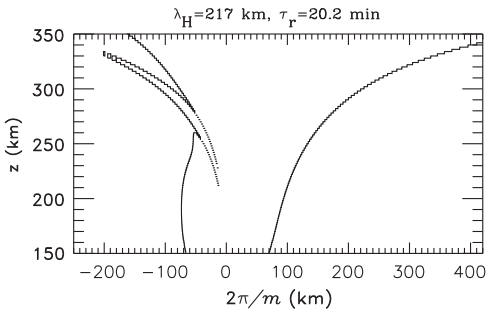

Fig. 1. Solution of the GW dispersion relation, Eq. (1), for a GW with $\lambda_H = 217$ km and $\tau_r = 20.2$ min in zero neutral, background winds, $U = V = 0$.

If this GW is upward propagating and dissipates at $z_{\mathrm{diss}} \sim 160$ km, then it is reasonable to ask what the GW λ_z solutions signify for $z > 260$ km. Suppose an upward- or downward-propagating GW with these values of λ_H and τ_r was created by some physical process at $z > 260$ km in the thermosphere. Then Fig. 1 shows this GW's vertical wavelength as a function of altitude as it propagates and dissipates. However, because $z_{\mathrm{diss}} \sim 160$ km, this GW (whether upward or downward propagating) would dissipate very rapidly after being created since z is more than a few density scale heights above z_{diss} (Vadas, 2007).

Until a GW begins to dissipate, its horizontal flux of vertical momentum times the mass density, $\overline{\rho}(\overline{u_H' w'})$, is approximately constant as it propagates through an atmosphere with vertically varying winds, where the overline denotes a temporal average over a wave period, u_H' is the GW's horizontal velocity in the direction of propagation, and $u_H' w'$ is the horizontal transport of vertical momentum flux. Although the momentum flux remains constant, a GW's horizontal and vertical perturbation velocities vary as the background winds vary with altitude. For example, if an upward- and eastward-propagating, non-dissipating GW encounters a westward wind, λ_H is constant while λ_z increases. Using the Boussinesq continuity equation, $\nabla \cdot \mathbf{v}' = 0$, which can be rewritten in Fourier space as $m\widetilde{w}' = -k_H \widetilde{u}_H'$, where $\widetilde{\ }$ denotes the Fourier transform, a GW's vertical velocity times $\sqrt{\overline{\rho}}$ increases when propagating in a direction opposite to the background

Author's personal copy

wind, since

$$\overline{\rho w'^2} \sim -(\lambda_z/\lambda_H)(\overline{\rho u'_H w'}). \tag{12}$$

On the other hand, if this GW encounters an eastward wind (in the same direction as the GW's propagation direction), then its vertical velocity decreases because λ_z decreases.

Because the velocity of a GW is needed to calculate the plasma response, we utilize the GW polarization relations. Using Eqs. (B5), (B4) and (23) from VF2005, the anelastic, dissipative, polarization relation relating the horizontal and vertical GW perturbation velocities is

$$\frac{\widetilde{w}_0}{\widetilde{u_{H0}}} = -\frac{k_H m}{m^2+1/4\mathrm{H}^2}\left[1-\frac{i(\mathbf{k}^2+1/4\mathrm{H}^2)(\omega_I-i\alpha\nu)}{2m\mathrm{H}k_H^2N^2} \times\left[\left(\frac{2}{\gamma}-1\right)\omega_I-\frac{i\alpha\nu}{Pr}\right]\right]. \tag{13}$$

Here, $\alpha \equiv -\mathbf{k}^2+1/4\mathrm{H}^2+im/\mathrm{H}$, $\omega_I=\omega_{Ir}+i\omega_{Ii}$ is the complex intrinsic frequency, $\widetilde{u_{H0}}$ is the GW's "scaled" horizontal perturbation velocity, and $\widetilde{w}_0$ is the GW's "scaled" vertical perturbation velocity. "Scaled" denotes that the GW velocities are multiplied by $\exp(-z/\mathrm{H})$ prior to taking their Fourier transform (see VF2005). Note that Eq. (13) reduces to the correct equation in the non-dissipative, Boussinesq limit: setting $H\to\infty$ and $\nu=0$, Eq. (13) becomes $\widetilde{w}_0 \simeq -(k_H/m)\widetilde{u_{H0}}$, which is simply the 2D Boussinesq continuity equation. Note that Eq. (13) is complex, indicating a possible phase difference between the GW horizontal and vertical velocity perturbations other than 0° or 180° when a GW is strongly dissipating. We then calculate the squared horizontal and vertical velocity spectral amplitudes via

$$\widetilde{u_{H0}}\widetilde{u_{H0}}^* = \left(\frac{\widetilde{w}_0}{\widetilde{u_{H0}}}\right)^{-1}\widetilde{u_{H0}}\widetilde{w}_0^*, \tag{14}$$

$$\widetilde{w}_0\widetilde{w}_0^* = \left(\frac{\widetilde{w}_0}{\widetilde{u_{H0}}}\right)\widetilde{u_{H0}}\widetilde{w}_0^*. \tag{15}$$

Here, the * denotes the complex conjugate.

3. GW measurements with PFISR

3.1. Experiment

As described in more detail in Nicolls and Heinselman (2007), the Poker Flat Advanced Modular Incoherent Scatter Radar (PFISR) system is located at the Poker Flat Research Range (65.13°N, 147.47°W) near Fairbanks, Alaska. PFISR is capable of pulse-to-pulse beam steering, thereby pointing essentially simultaneously at multiple positions in the sky. The beam configuration for a recent experiment that exhibits good spatial coverage is shown in the lower right corner of Fig. 2, which shows the geographic beam positions (distance from the radar) at 200 km altitude. This configuration includes 10 beams spread in azimuth-elevation as well as a beam pointed nearly parallel to the local magnetic field line. Beam #8 is vertically pointed, and beam #10 looks up the local magnetic field line. For the observations presented in this paper, a 480 μs (72 km) long pulse was transmitted on two frequencies, and sampled every 30 μs (4.5 km).

3.2. Density measurements

The radar samples complex voltages as a function of range associated with incoherent backscatter (IS). These returns can be used to form complex autocorrelation functions (ACFs), related to the power spectrum by a Fourier transform. ACFs can be fit for common IS parameters such as electron density (N_e), electron temperature (T_e), ion temperature (T_i), and the line-of-sight (LOS) ion speed (V_{los}) (e.g., Evans, 1969), although typically to obtain absolute electron density requires a calibration (a task for PFISR which is performed using supplementary plasma line measurements). Backscattered power is related to electron density by a simple relation (valid for $T_e/T_i \sim \leqslant 4$) (e.g., Evans, 1969),

$$P_r = \frac{P_t\tau_p}{R^2}K_{sys}\frac{N_e}{(1+k^2\lambda_D^2)(1+k^2\lambda_D^2+T_e/T_i)}, \tag{16}$$

where P_t is the peak transmit power (~1.3 MW for the experiment described in this paper), τ_p is the pulse length, R is range, K_{sys} is a system constant that encompasses gain and other effects, $k=4\pi/\lambda \sim 18.8\,\mathrm{m}^{-1}$ is the radar Bragg wavenumber, and $\lambda_D \sim 69\sqrt{T_e/N_e}$ is the electron Debye length. For the PFISR probing frequency of ~450 MHz, the Debye length term can be neglected for densities above a few times $10^{10}\,\mathrm{m}^{-3}$, and we are left with a correction term due to the electron-to-ion temperature ratio.

For an uncoded pulse of length τ_p, the power measurement is range smeared over the length of the pulse, so that the measured power (P_r^M) at range R is related to the true power (P_r) by

$$P_r^M(R) = \int_{R-c\tau_p/4}^{R+c\tau_p/4} P_r(R')\,dR', \tag{17}$$

where c is the speed of light.

If we assume that T_e/T_i is roughly constant over the length of the pulse, a reasonable assumption in the F region, then we can write a similar expression for the measured electron density,

$$N_e^M(R) = R^2\int_{R-c\tau_p/4}^{R+c\tau_p/4}\frac{N_e(R')}{R'^2}\,dR'. \tag{18}$$

Measured electron densities in the presence of GWs may be expressed as a superposition of a background ($\overline{N}_e$) and a perturbation (δN_e) quantity, i.e.,

$$N_e(R) = \overline{N}_e(R) + \delta N_e(R), \tag{19}$$

so that Eq. (18) becomes

$$N_e^M(R) = R^2\int_{R-c\tau_p/4}^{R+c\tau_p/4}\frac{\overline{N}_e(R')+\delta N_e(R')}{R'^2}\,dR'. \tag{20}$$

The measured fractional perturbation in electron density, then, is computed as

$$\frac{\delta N_e^M(R)}{\overline{N}_e^M(R)} = \frac{N_e^M(R)}{\overline{N}_e^M(R)} - 1, \tag{21}$$

which includes the range-smearing effects of the long pulse.

For the results presented in this paper, T_e/T_i variations associated with the passage of a GW are neglected. This assumes that electron density variations are proportional to variations in backscattered power. While (T_e/T_i)-induced variations change the magnitude of $\delta N_e/N_e$, only variations of the relative phases of δT_e and δT_i with altitude affect the results derived in this paper. The inferred electron density variations are related to the true electron density variations by the expression

$$\frac{\delta P_r}{P_r} = \frac{\delta N_e}{N_e} - \frac{\delta T_e}{T_e}\frac{T_e/T_i}{1+T_e/T_i}\phi_{T_e} + \frac{\delta T_i}{T_i}\frac{1}{1+T_e/T_i}\phi_{T_i}, \tag{22}$$

where ϕ_{T_e} and ϕ_{T_i} represent the phase difference between the temperature perturbations and the electron density perturbations. By neglecting the temperature phase variations, we are making the assumption that the amplitude of the temperature perturbations (modified by the given factors) is small compared with the density perturbations and/or that the phase variations of those perturbations do not change with altitude. Although some studies have shown that the phase of the temperature perturbations is different and change with altitude (e.g., Hocke et al., 1996),

Author's personal copy

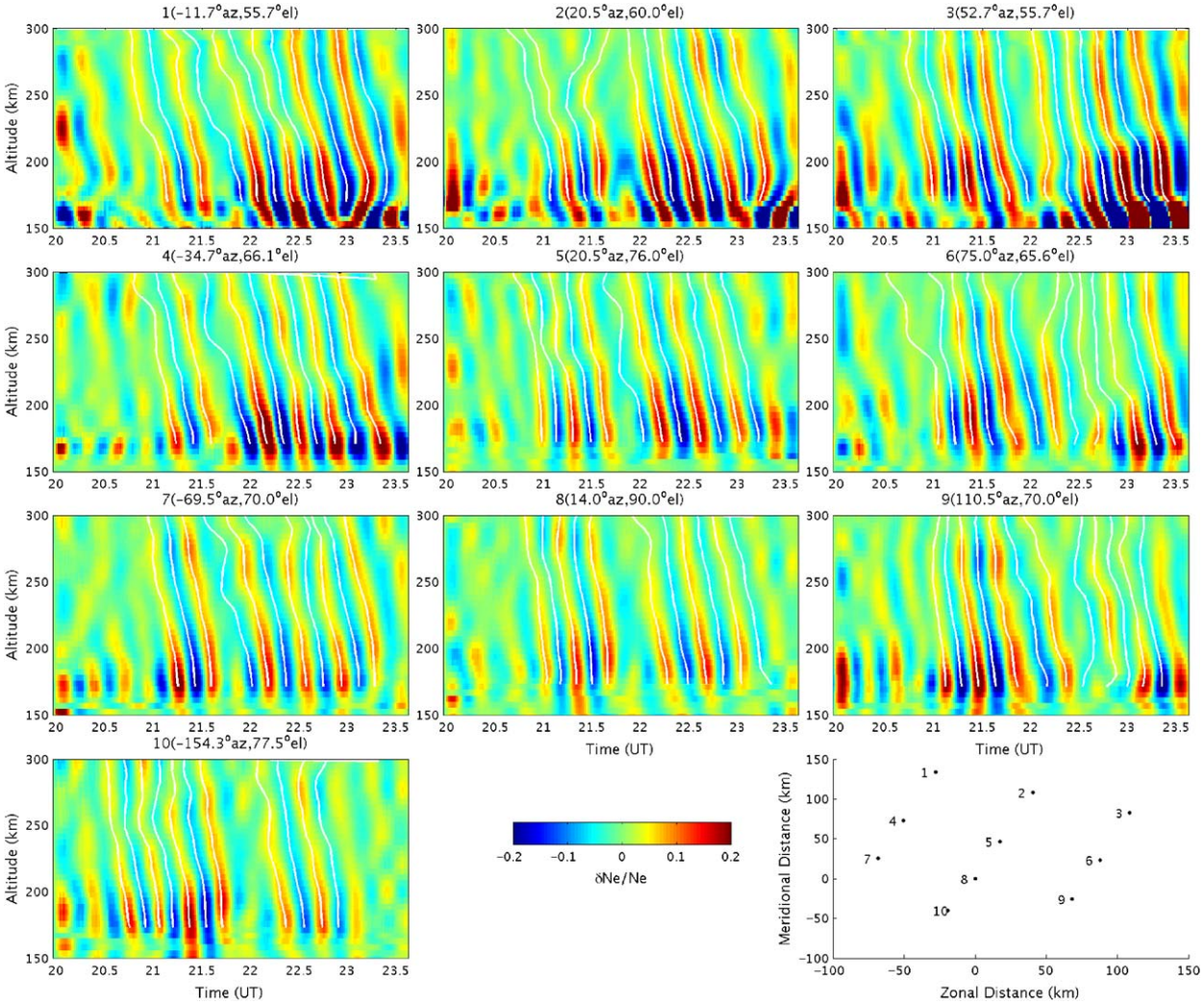

Fig. 2. Electron density fractional perturbations for all 10 beams as a function of time and altitude on 13 December 2006. The lower right panel shows beam positions at an altitude of ~200 km.

at lower altitudes ($\sim<250$ km) both electron and ion temperature perturbations are expected to be strongly coupled to neutral temperature perturbations; therefore, assuming that $\delta T_e \approx \delta T_i \approx \delta T_n$ is a reasonable approximation (Hocke et al., 1996; Testud and Francois, 1971). In addition, the perturbation amplitudes of the T_e and T_i fluctuations are expected to be considerably smaller than those of the N_e perturbations (e.g., Kirchengast, 1996), and are further reduced by the fact that $T_e/T_i>1$ during the daytime. Nevertheless, this is a potential source of error in the analysis and could affect the derived results, in particular the magnitude of the electron density perturbations. While we did derive temperatures for this experiment, they are not sufficiently precise to determine the δT_i and δT_e phase relationships accurately as a function of altitude needed to extract the horizontal winds (see Section 4). We do note, however, that we have found that including them does not significantly change the shape and amplitudes of the extracted winds, although the errors are much larger.

More importantly, the range smearing induced by the long pulse and implied by Eq. (20) can have a significant impact on the inferred phase variations of δN_e. Thus, some mitigation of this effect is necessary; more recent experiments have employed experimental techniques that minimize this effect. The approach taken here is to first compute δN_e^M and $\overline{N}_e^M$, i.e., the range-smeared density perturbation and background density, respectively, by filtering the measured densities; this procedure is described in more detail below. These quantities are then deconvolved to determine an estimate of the true background and perturbation densities. The deconvolution is regularized using a smoothness constraint that penalizes large gradients in the solution. An illustrative example of this process is shown in Fig. 3. Fig. 3a shows a typical N_e measurement (black), which has errorbars (statistical fluctuations) of 5–7% in the altitude range of interest. The gray line here shows the resultant background density ($\overline{N}_e^M$) determined from the filtering process. The black solid line in Fig. 3b also shows the measured δN_e^M. All three of these quantities suffer from range smearing. Deconvolution gives the solid blue line in the middle panel; the solid gray line results after applying the forward model, which matches very well with the observed δN_e^M (although it is much smoother, as a result of the applied regularization). Note that the main result of this process is an increase in amplitude of the density perturbation, and a small shift in peak altitude, both of which are expected given the characteristics of the range smearing. The right panel shows the resultant $\delta N_e/N_e$, which are then used in our analysis to compute the GW vertical wavelengths, as described next.

The $\delta N_e/\overline{N}_e$ inferred using this procedure on 13 December 2006 is plotted in Fig. 2, for all beam directions. The densities here have been integrated for approximately 1 min. Prior to applying

Author's personal copy

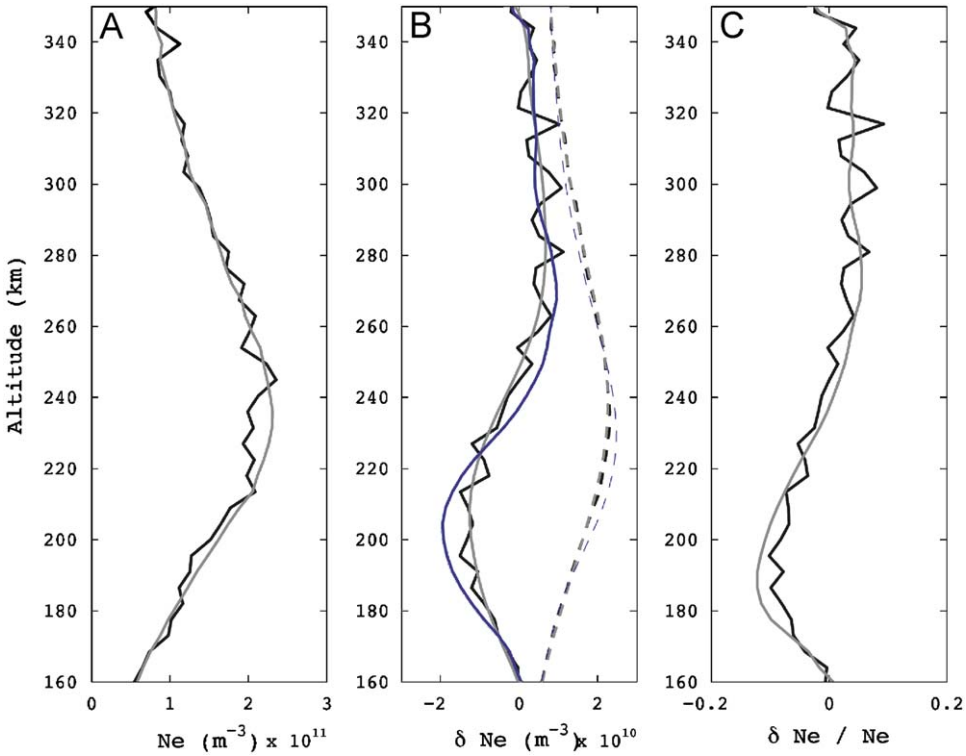

Fig. 3. (a) Measured N_e (black) and extracted $\overline{N}_e^M$ (gray). (b) Extracted δN_e^M (black solid) and forward model (gray solid), with resultant δN_e (blue solid). Same for $\overline{N}_e^M$ (dashed), which have been scaled by a factor of 10. (c) Resultant $\delta N_e/N_e$, without range correction (black) and after deconvolution (gray).

the deconvolution procedure, the data were zero-phase filtered with a sixth-order Butterworth bandpass filter, which was designed to remove signals outside of the 10–40 min passband while losing no more than 3 dB in the passband, and having an attenuation of at least 15 dB in the stopband. In this way, estimates of both δN_e and $\overline{N}_e$ were produced. Two distinct GWs are discernible in the figure during the time period from 20:00 to 24:00 UT (local standard time is LST = UT − 9), although they have similar periods. The first GW can be seen from 20:00 to 22:00, while the second GW can be seen from 22:00 to 24:00 UT. Note that the latter GW was investigated by Nicolls and Heinselman (2007), and changes with altitude of its vertical wavelength were used to compute the vertical variations of the average neutral background wind in Vadas and Nicolls (2008), although the range-smearing corrections described in this section were not applied to those calculations. The thin white lines in Fig. 2 trace lines of constant wave phase, where the absolute value of the electron density perturbation is maximum. We will show later how diagnosing these lines of constant wave phase yields important information on the temporal variability of the background winds through which the GWs propagate.

Several important features are apparent in Fig. 2. First, the positive and negative oscillations of the electron density perturbations are fairly periodic in all of the beams. Second, the wave phases for all of the GWs move downward in time, indicating upward-propagating GWs from Eq. (7), since $m<0$ for upward-propagating GWs when dissipation can be neglected. Third, the electron density perturbations are maximum at $z\sim180-200$ km, where $\overline{N}_e$ changes rapidly (see Fig. 1 from Vadas and Nicolls, 2008). This seems to suggest that the GWs dissipate at $z\sim190$ km. However, the altitude where $\delta N_e/\overline{N}_e$ peaks is not equal to the altitude where the GW's momentum flux is maximum; rather, the electron density responds most strongly to rapid changes with altitude in the background electron density and/or the GW amplitude (see Section 5). Fourth, these waves are relatively high frequency; the first GW's period is ~20 min, while the second GW's period is ~24 min. In order to see that these GWs are two different waves, we highlight the time difference between the electron density perturbations where there is a "gap" in GW activity. In beam #8, for example, the time difference between the dark blue contours at 21:29 and 22:27 UT at $z\sim180$ km is 58 min.

The positive and negative electron density perturbations at a given altitude occur at different times in the different beams. This is because the GWs are propagating horizontally and vertically through the beams at differing times, since these beams are spread out horizontally in the thermosphere (see lower right panel of Fig. 2). For example, note that beams #4 and 7 are northwest (NW) of the vertical beam (#8), while beam #9 is SE of the vertical beam. Thus if a GW is propagating SEward, it will reach beam #4 first, then #7, then #8, and finally #9. Using the horizontal spacing between the beams and the GW period, the horizontal phase speeds, wavelength, and propagation directions of the GWs can be computed from Fig. 2. GW#2 was found to be propagating SEward (Nicolls and Heinselman, 2007; Vadas and Nicolls, 2008). This direction of propagation is confirmed via a different PFISR measurement. Fig. 4 shows very precise plasma line measurements of the peak electron density using a plasma line cutoff technique (e.g., Showen, 1979) from 5 of the 10 beams where the plasma line was detected. The plasma line densities in Fig. 4a show clear density perturbations of roughly the same magnitude as observed in the power measurements of Fig. 2. The power spectra in Fig. 4b show that ~20−25 min waves are clearly present. The density perturbations are shown in Fig. 4c as a function of time and horizontal distance for 3 beams each in the approximately zonal (left) and meridional (right) directions. From Fig. 4c, it is clear that the wave is propagating eastward and southward.

Author's personal copy

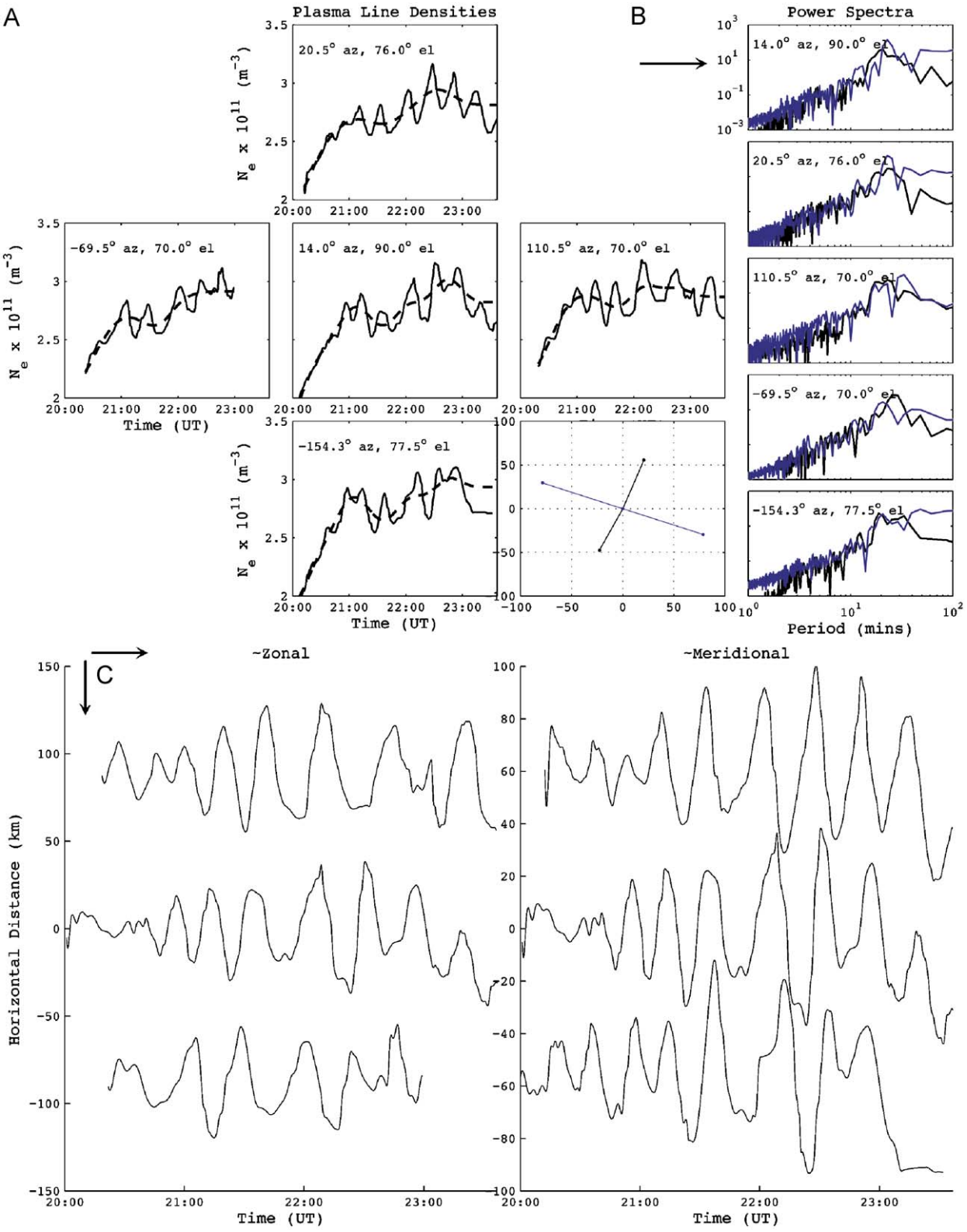

Fig. 4. Summary of plasma line observations from five beams where the line was detectable. (a) Electron densities inferred from the plasma lines for all five beams (solid), along with the estimates of $\overline{N}_e$ (dashed lines). The lower right-hand corner shows the geometry plot of these beams. (b) Power spectra for each of the beams in (a), as labeled. (c) $\delta N_e/\overline{N}_e$ for the three beams aligned in the approximately zonal direction (blue line in the geometry plot in (a)) and the meridional direction (black line in the geometry plot in (a)).

In Table 1, we show the extracted GW parameters. The columns from left to right show the number of the wave, the time (in UT), λ_x, λ_y, λ_H (in km), $\tau_r = 2\pi/\omega_r$ (in min), and the propagation angle clockwise from north, $\psi = 90 - \tan^{-1}(\lambda_x/\lambda_y)$ (in deg). Horizontal wavelengths were determined by examining the "propagation" of density perturbation peaks through chosen beams. This procedure is illustrated in Fig. 5. Here, we show perturbations observed along 6 "rows" of beams that are horizontally aligned at an

Author's personal copy

altitude of ~200 km. Rows consisting of beams (1,4,7), (2,5,8,10), and (3,6,9) form a line at an angle that is approximately 20° east of north. Beams (1,2,3), (4,5,6), and (7,8,9), on the other hand, form a line at an angle that is approximately −70° west of north. Because these lines are nearly perpendicular, they provide accurate estimates of the direction of propagation and horizontal wavelengths of the GWs. It is clear from Fig. 5 that both waves are propagating southward and eastward. Using the inferred perturbation speeds from Fig. 5, we derive a single horizontal phase speed along each direction, and an associated error estimate, and utilize these results to derive an estimate of the horizontal wavelengths in geographic coordinates. The first GW was propagating SEward, ~38° counterclockwise from south, with a horizontal phase speed of $c_H = \omega_r/k_H = 179$ m/s. The second GW was propagating SEward, ~27° counterclockwise from south, with a horizontal phase speed of $c_H = \omega_r/k_H = 141$ m/s. These speeds are smaller than ~250 m/s, and suggest that these GWs originated in the lower atmosphere. Note that Table 1 does not contain λ_z values for these GWs, because λ_z varies with altitude due to the spatially and temporally varying background, neutral, horizontal winds. Vertical wavelengths of these GWs will be calculated in Section 4, and will be utilized as tools to determine the spatial and temporal variability of the background, neutral winds.

Fig. 6 shows bandpass filtered LOS ion velocities, δV_{los} from all 10 beams. These measurements indicate that δV_{los} are small, 10–20 m/s, as were the un-filtered velocities, indicative of small

Table 1
Gravity wave parameters.

Wave	Time (UT)	λ_x (km)	λ_y (km)	λ_H (km)	τ_r (min)	ψ (deg)
#1	20:00–22:00	349 ± 15	-277 ± 10	217 ± 6	20.2 ± 0.2	$142 \pm 3°$
#2	22:00–24:00	451 ± 53	-226 ± 13	202 ± 11	23.9 ± 0.1	$153 \pm 3°$

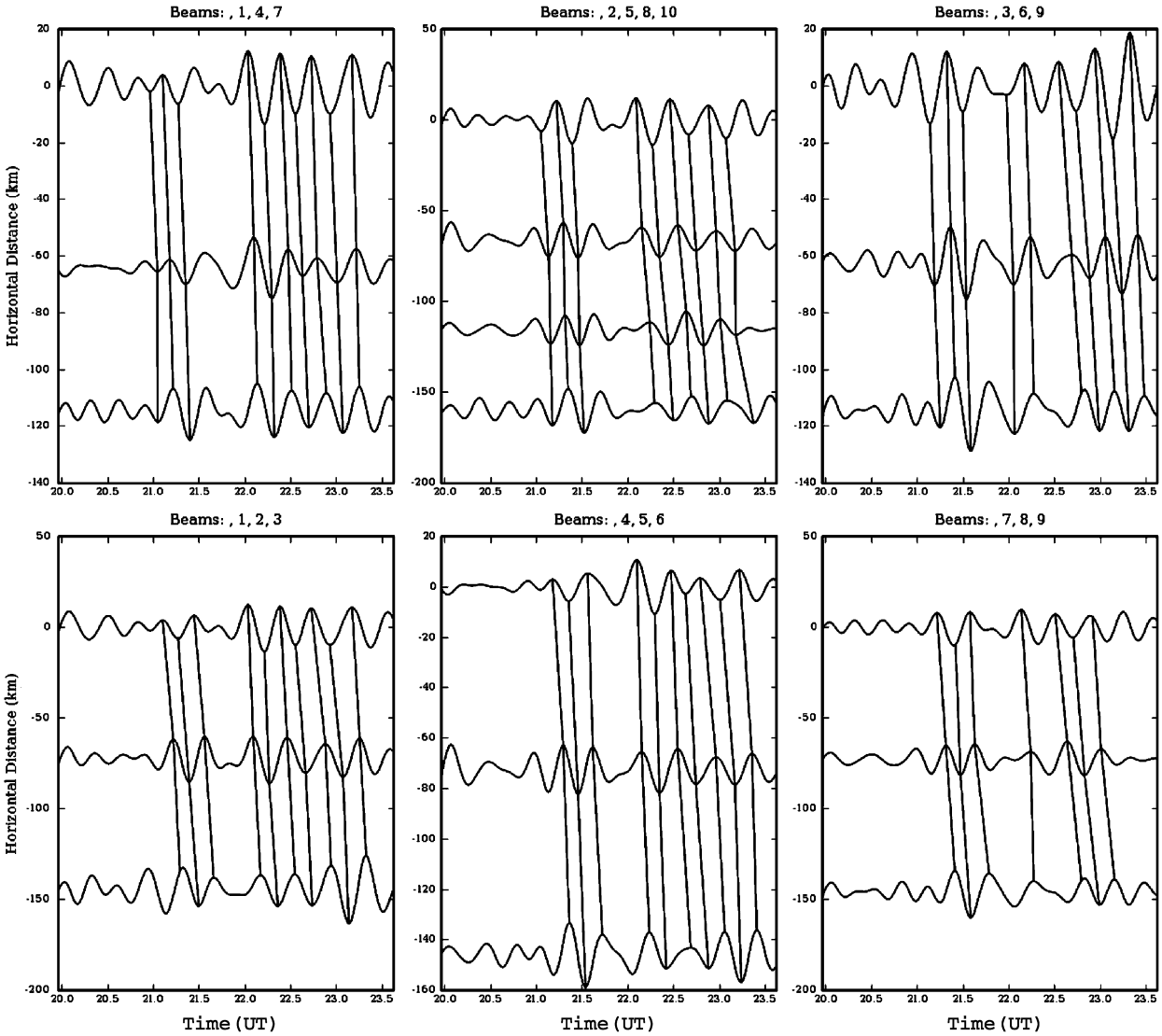

Fig. 5. Density perturbations as a function of time and horizontal distance for three or four beams, as labeled, referenced to the first beam. Solid lines denote the paths of phase propagation. In the top row, beams are aligned northern-most to southern-most (from top to bottom), whereas in the bottom row they are aligned from western-most to eastern-most (top to bottom).

Author's personal copy

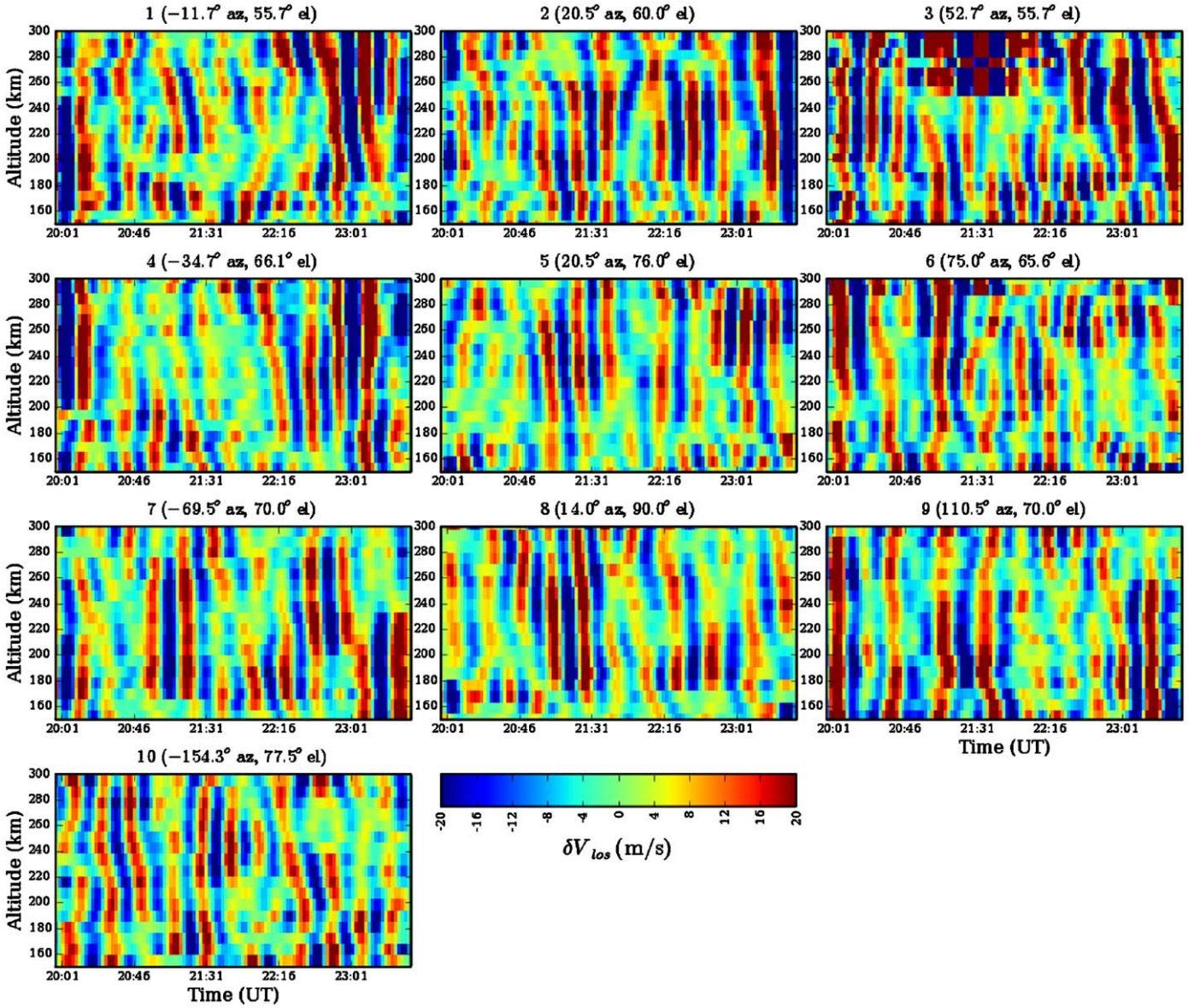

Fig. 6. Low and high bandpass filtered line-of-sight ion velocities, V_{los}, for all 10 beams.

electric fields and low geomagnetic activity. The plasma oscillations are induced by the GWs via neutral-ion collisions. Because the ions are confined to move along the magnetic field line, the V_{los} perturbations looking up the magnetic field line (beam #10) approximately equals the GW vertical velocity, w', since the magnetic field is nearly vertical at Poker Flat (PF), with a dip angle $I = 77.5^{\circ}$. We therefore estimate a GW vertical velocity of $w' \sim 15-20\,\mathrm{m/s}$ for these GWs at $z \sim 220\,\mathrm{km}$.

There are several other features to note about Fig. 6. First, the positive and negative oscillations of V_{los} are fairly periodic in all of the beams. Second, we can clearly see both GWs, separated by the same "gap" in significant GW activity as in Fig. 2. Third, the constant phase lines of V_{los} and $\delta N_e/N_e$ are offset in time. For many of the phase lines, V_{los} lags $\delta N_e/N_e$ in phase by approximately 90°. When V_{los} and $\delta N_e/N_e$ are in quadrature, advection is the most important contributor to the ion continuity equation (see Section 5). However, other investigators have found larger GW phase differences of 180−210° at $z \sim 200-250\,\mathrm{km}$ from the EISCAT data (Kirchengast et al., 1996), and variable phase differences of 90−180° were found for GWs detected by the Dynamics Explorer-2 satellite data (Earle et al., 2008). Phase differences other than 90° can occur when other processes such as chemical, ion drag, neutral-ion heating, and ion friction are important (Kirchengast et al., 1996). Fourth, rather than peaking at $z \sim 190\,\mathrm{km}$ like the electron densities, V_{los} peaks at much higher altitudes, at $z \sim 200-260\,\mathrm{km}$ (see Section 5). This behavior has been researched previously (e.g., Kirchengast et al., 1996).

3.3. GW lines of constant phase for determining λ_z

In this subsection, we show how a GW line of constant phase is related to the vertical wavelength. A GW's amplitude is oscillatory, and is proportional to

$$\exp[i(kx + ly + mz - \omega_r t)] = \exp[i(\mathbf{k}\cdot\mathbf{x} - \omega_r t)] = \exp(i\phi), \qquad (23)$$

where $\phi = kx + ly + mz - \omega_r t$ is the phase of the wave and $\mathbf{x} = (x, y, z)$ is a cartesian vector. Thus, the absolute value of the GW's amplitude is largest when $\phi = 0, 2\pi, 4\pi, \ldots$ (positive) and $\phi = \pi, 3\pi, 5\pi, \ldots$ (negative). The electrons and ions respond to this GW

Author's personal copy

by oscillating in time and in space (Klostermeyer, 1972; Kirchengast et al., 1996). We assume that the electron density perturbations created by this GW follow the same functional behavior as Eq. (23), with the addition of an arbitrary phase shift. We will show in Section 5 that this assumption is approximately true for a single-ion species where chemical and drag effects can be neglected. Because O^+ is the dominant species above $z\sim200$ km, this analysis is likely more accurate above $z\sim200$ km than below $z\sim200$ km.

For a radar beam pointing at azimuth ζ (clockwise from north) and elevation θ (from horizontal), the cartesian vector in a radar-center geographic coordinate system (neglecting earth-curvature effects) is

$$\mathbf{x} = R\mathbf{A}, \tag{24}$$

where

$$\mathbf{A} = \cos\theta\sin\zeta\hat{\mathbf{i}} + \cos\theta\cos\zeta\hat{\mathbf{j}} + \sin\theta\hat{\mathbf{k}} \tag{25}$$

is the unit vector in the beam look direction, R is the range, and $\hat{\mathbf{i}}, \hat{\mathbf{j}}$, and $\hat{\mathbf{k}}$ are the unit vectors in the zonal, meridional and vertical directions, respectively. Then, the variation in ϕ along a constant wave phase line is

$$d\phi = k\,dx + l\,dy + m\,dz - \omega_r\,dt = (\mathbf{A}\cdot\mathbf{k})\,dR - \omega_r\,dt = 0. \tag{26}$$

This implies a slope of the constant phase line of

$$\left.\frac{dR}{dt}\right|_\phi = \frac{\omega_r}{\mathbf{A}\cdot\mathbf{k}}, \tag{27}$$

where "$|_\phi$" indicates that the derivative is taken with ϕ constant. Note that we can write Eq. (27) in terms of altitude, $z = RA_z$, by multiplying both sides by A_z,

$$\left.\frac{dz}{dt}\right|_\phi = \frac{\omega_r}{\frac{A_x}{A_z}k + \frac{A_y}{A_z}l + m} = \frac{\omega_r}{m}\left(\frac{1}{\mathbf{A}_H\cdot\mathbf{k}_H/(A_z m) + 1}\right), \tag{28}$$

where $\mathbf{A}_H$ and $\mathbf{k}_H$ are the horizontal components of $\mathbf{A}$ and $\mathbf{k}$, respectively. If the term $\mathbf{A}_H\cdot\mathbf{k}_H$ is close to $-A_z m$, then the denominator of the correction term in Eq. (28) tends to zero, yielding a very large vertical wavelength. In this case, however, the large λ_z is not due to a change in the background winds (as it is for a vertically pointed beam—see below), but rather because the radar beam is pointing perpendicular to the $\mathbf{k}$-vector of the GW, i.e., $\mathbf{A}\cdot\mathbf{k}\simeq 0$. For the upward-propagating GWs we analyze here, the $\mathbf{k}$-vectors point downwards, along the constant phase lines. For a non-vertically pointing radar beam $\mathbf{A}$, the beam may be perpendicular to $\mathbf{k}$ at specific altitudes and times. At these fairly rare times, the calculated values of λ_z are very large. This would seem to present a problem when extracting the background winds from profiles of the vertical wavelength. However, it turns out not to pose a significant problem, because the extracted background winds only depend on $m = 2\pi/\lambda_z$; when λ_z gets very large and $m^2 \ll k_H^2 + 1/4\mathrm{H}^2$, the value of m has little effect on the extracted horizontal, neutral wind. Thus, we need no special analysis when $\mathbf{A}\cdot\mathbf{k}\simeq 0$.

If we solve Eq. (28) for the vertical wavelength, we obtain

$$\lambda_z = \frac{2\pi A_z}{\omega_r\left(\left.\frac{dR}{dt}\right|_\phi\right)^{-1} - \mathbf{A}_H\cdot\mathbf{k}_H}. \tag{29}$$

Thus, by measuring the slope of a line of constant wave phase, we can determine λ_z for an assumed fixed horizontal wavelength.

For fixed x and y (i.e., a vertically pointing beam), $\theta = 90^\circ$, and Eq. (28) becomes

$$\left.\frac{dz}{dt}\right|_\phi = \frac{\omega_r}{m}. \tag{30}$$

For this special example, the vertical wavelength is easily calculated:

$$\lambda_z = \tau_r\left(\left.\frac{dz}{dt}\right|_\phi\right). \tag{31}$$

Since the ground-based period τ_r is assumed constant, any changes in time or altitude in the slopes of the constant wave phase lines for the vertical beam, $(dz/dt)|_\phi$, are due to the variation of the GW's vertical wavelength with altitude and/or time.

4. Temporal evolution of the thermospheric, neutral winds

Vadas and Nicolls (2008) analyzed the GW that was observed by PFISR from 22:00 to 24:00 UT on 13 December 2006; this is the same as GW #2 we analyze here. They calculated a mean λ_z profile with altitude by averaging over most of the time that this GW was observed. They used this mean profile to extract an average, background, neutral, horizontal wind along the direction of GW propagation using the GW dissipative dispersion relation. (Note, Vadas and Nicolls, 2008, did not account for range-smearing and other effects, as we have done here.) Along with the mean component of the anti-parallel ion velocity, V_{ap} (which was used to estimate the neutral wind along the magnetic meridian, U_m), they determined that the neutral wind was quite strong from $z =$ 180 to 200 km, and was directed opposite to the GW's propagation direction, towards the NW. However, calculating an averaged-in-time λ_z profile resulted in a loss of information about the temporal evolution of the background winds. Because we wish to understand how the winds evolve in time, we determine the time-evolution of both GW's λ_z profiles using the slopes of their constant wave phase lines and Eq. (29). Then, knowing that λ_z evolves in time because of Doppler shifting as a GW propagates through temporally and spatially varying background winds, we can extract the background, neutral winds every one-half wave period, or every $\tau_r/2\sim10-12$ min, in each of the beams.

4.1. Determination of the GW vertical wavelengths

There are five significant positive and negative constant wave phases for beam #8 where $|\delta N_e/\overline{N}_e|$ is maximum. The times and altitudes where this occurs are shown in Fig. 7 as dashed lines; these are equivalent to 10 of the thin white lines in Fig. 2. We also apply a three-point running average to these lines, and plot them as solid lines in Fig. 7. These solid lines are used to determine the derivative of altitude with respect to time along constant wave phase lines, $(dz/dt)|_\phi$. Note that $(dz/dt)|_\phi$ is nearly vertical for some of the phase lines at $z\sim180-200$ km.

Using Eq. (29), we show offsetted profiles of λ_z as a function of altitude for all 10 wave constant phase lines in Fig. 8a. Here, a three-point running average has been applied to the calculated $|\lambda_z|$ profiles. The hatched region with dashed lines separates GWs #1 and 2. Because λ_z switches sign occasionally where $z(t)|_\phi$ is approximately vertical, and because the non-dissipative dispersion relation only depends on m^2, we plot the absolute values of λ_z (with the same three-point running average) in Fig. 8b for GWs #1 and 2. First, we note that λ_z can be large at $z\sim180-200$ km, i.e., $\lambda_z \to 200-300$ km. These large values of λ_z occur where the GW becomes nearly evanescent or evanescent; at this altitude, a portion of the GW likely reflects downwards. However, because δV_{los} peaks at somewhat higher altitudes for these phase lines (see Fig. 6), if the GW is evanescent, then it must be tunneling through the barrier to $z\sim200$ km where it is no longer evanescent. Tunneling may be possible for this GW because the vertical scale over which evanescence occurs, $\Delta z\sim20$ km, is much smaller than

Author's personal copy

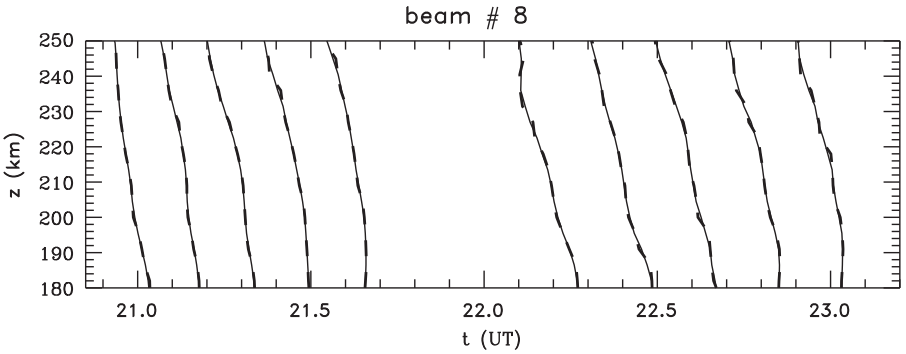

Fig. 7. Times where the GW phases are maximum as a function of altitude for beam #8 (dash lines). Three-point running average of the same times (solid lines).

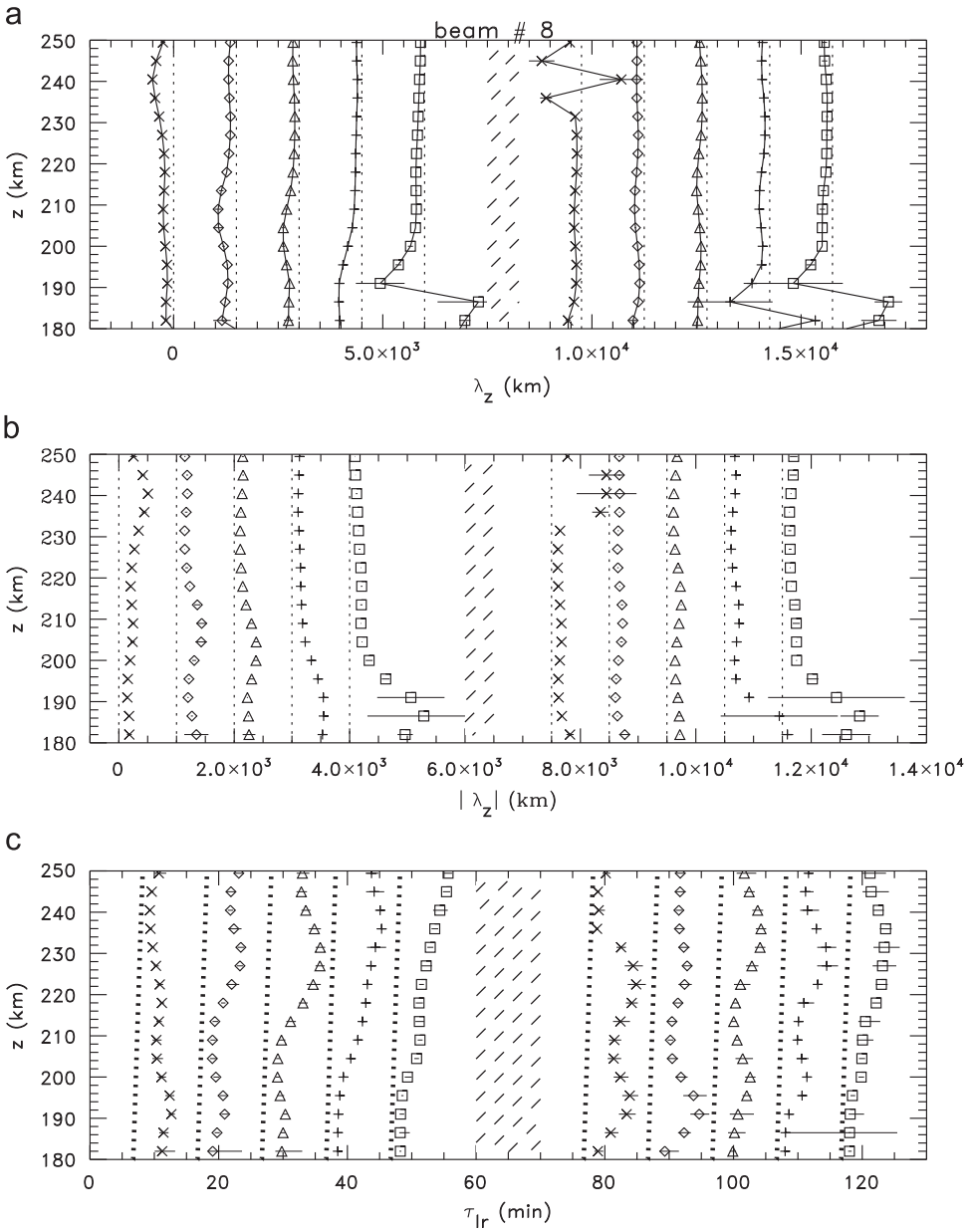

Fig. 8. (a) Values of $\lambda_z(z)$ computed from Eq. (29) using the solid lines in Fig. 7 for both GWs in beam #8. The $\lambda_z(z)$ profiles are offsetted by 1500 km. The results along the first, second, third, forth and fifth constant wave phase lines are shown as ×'s, diamonds, triangles, +'s, and squares, respectively. The following five phase lines repeat these symbols. The dot lines show $\lambda_z = 0$ for each constant phase line. The hatched regions with dashed lines separate GWs #1 and 2. (b) Same as in (a), but showing $|\lambda_z(z)|$ instead. The profiles are offsetted by 1000 km. (a) Computed values of the intrinsic period via solving Eq. (1) iteratively. Profiles are offsetted by 10 min, and use the same symbols as in (a). The buoyancy period, $2\pi/N$, is shown as dotted lines.

Author's personal copy

the GW's vertical wavelength. Second, λ_z varies in time and in altitude. When this occurs and the GW is not yet dissipating, the neutral background winds must be changing in time and in altitude. Third, when a GW is dissipating, λ_z will vary irrespective of the winds (VF2005).

4.2. Extracting the neutral winds from the vertical wavelength profiles

We now calculate the intrinsic frequency profiles from Eq. (1). This requires the background neutral temperature profile, $\overline{T}(z)$. Because we do not know this temperature profile, we utilize $\overline{T}(z)$ from the empirical NRLMSISE-00 model (Hedin, 1991). Note that it was estimated that a 20% uncertainty of $\overline{T}$ results in a 15% uncertainty of the extracted neutral wind (Vadas and Nicolls, 2008). Geomagnetic activity on and around 13 December 2006 was quite low, with a daily sum Kp index of 13.3 (daily average Ap index of 8) for the day of observation and no significant geomagnetic storms in the several days prior to the observation period. The $\overline{T}(z)$ profile was shown in Fig. 2c in Vadas and Nicolls (2008), and has a maximum thermospheric temperature of $\overline{T}\sim$810 K. We also set $Pr = 0.7$ and $\mu = 3.34\times10^{-4}\overline{T}^{0.71}$ gm/m/s. Using the $\lambda_z(z)$ data from Fig. 8a with a three-point running average, we solve Eq. (1) iteratively for $\omega_{Ir}(z)$ starting at the lowest altitude where ν is negligible, and use the ω_{Ir} solutions as initial guesses as z is increased. Here, λ_H and ω_r are taken to be constant, which assumes that horizontal and temporal variations of the background winds and temperature are "small" along ray paths. Fig. 8c shows the intrinsic wave period, $\tau_{Ir} = 2\pi/\omega_{Ir}$, as a function of altitude for all 10 phase lines. Note that τ_{Ir} varies with altitude and time.

We also plot the buoyancy period from the MSIS model, $\tau_B = 2\pi/N(z)$, as dot lines. We see that τ_{Ir} is nearly equal to τ_B at $z\sim$180−200 km for the phase lines where λ_z is very large. This is because if $\tau_{Ir} = \tau_B$, then $m = 0$ and $\lambda_z \to \infty$. Since λ_z switches sign for many of the phase lines at $z\sim$180−200 km in Fig. 8a, it is likely that these GWs were evanescent over that altitude range for at least some of the time. In this case, τ_{Ir} should equal τ_B at those altitudes; however, τ_{Ir} is shown to be ∼1 min larger than τ_B in Fig. 8c. Therefore, the actual thermospheric temperature over PFISR may have been somewhat larger than that given by MSIS.

From Eq. (2), the background, neutral wind along the direction of propagation of the GW can be extracted from the intrinsic and observed wave periods via

$$U_H(z) = \lambda_H\left(\frac{1}{\tau_r} - \frac{1}{\tau_{Ir}}\right). \tag{32}$$

Fig. 9a shows the resulting extracted, horizontal winds in beam #8 for GWs #1 and 2. A negative value indicates that the wind is opposite to the propagation direction of the GW. Since both GWs propagate to the SE, and because the extracted winds in Fig. 9a are negative, the projection of the background, neutral wind along the NW–SE direction is always NW for beam #8. Additionally, Vadas and Nicolls (2008) estimated that the total, horizontal neutral wind (not just the projection in the NW–SE direction) was in the NW direction, using the mean component of the anti-parallel ion velocity. Note that when the extracted wind amplitudes are close to ∼300 m/s, the actual background winds may be larger, because there is an upper limit to the extracted wind amplitude with this method. This limit is based on the GW's horizontal wavelength and period (see Eqs. (33) and (34)).

Fig. 9a shows that the extracted winds contain an oscillation with a 35–40 km vertical scale. We apply a nine-point running average to Fig. 9a to remove this oscillation from the winds. Fig. 9b shows these smoothed winds. These winds are to the NW, and change slowly with time and altitude. For most of the phase lines, the wind amplitude decreases steadily with altitude, with $U_H\sim -$(150−250) m/s at lower altitudes and $U_H\sim -$(75−150) m/s at higher altitudes.

For each constant phase line, we calculate the average of the smoothed winds in Fig. 9b from $z = 180$ to 250 km. These mean winds will be shown in the next figure, and have amplitudes of $\overline{U_H}\sim -$(140−170) m/s. We then subtract these mean winds from the smoothed winds, and show the residual winds in Fig. 9c. We see a deep, slowly moving wave with an amplitude of $U_H\sim$(50−75) m/s in most of the phase lines. This wave is upward-moving, because its phase descends slowly in time, as can be seen from phase lines 2–5. For the third and fourth phase lines, it is easy to see that the altitude where the wave is maximum negative and positive is $z\sim$190 and 230−240 km, respectively, implying an approximate vertical wavelength of $\lambda_z\sim$80−100 km for this slowly moving wave. Note that this slowly moving wave increases the NW mean wind at $z\sim$190 and decreases the NW wind at $z\sim$230−240 km, thereby changing the total wind field that GWs #1 and 2 propagate through.

In Fig. 9d, we show the extracted winds from Fig. 9a minus the smoothed background winds from Fig. 9b in order to examine the oscillations in more detail. The oscillations appear to be approximately stationary with time, with amplitudes of $U_H\sim$50−75 m/s. If these oscillations occurred because of the presence of an additional GW, then its period would have to be 10–12 min, which is the approximate time between the phase lines, and its vertical wavelength would have to be $\lambda_z\sim$35−40 km. We note that GWs with $\lambda_z <$ 70 km are not believed to be able to reach altitudes of $z\sim$220−240 km because of dissipative filtering (Vadas, 2007; Fritts and Vadas, 2008). Therefore, we are skeptical that this oscillation represents a true GW; it may be an artifact of the data processing, in particular the deconvolution of the range-smearing effects of the long pulse, as described in Section 3.

In Fig. 10, we show the mean U_H as a function of the mean time, which is the average from $z = 180$ to 250 km of the smoothed wind in Fig. 9b. We note that the strength of the mean wind increases from $\overline{U_H}\sim -140$ to −170 m/s from 21:00 to 23:00 UT. However, there is variability in these mean winds of order ±10 m/s. Because the mean horizontal wind is slowly varying with time over this 2-h window, it is likely due to a wave with a period larger than ∼8 h. The dominant tidal modes in the thermosphere are migrating diurnal and semi-diurnal tides, with the latter dominating in the lower thermosphere and the former dominating at altitudes above ∼200 km (Forbes, 1995). Note that global circulation models predict the amplitudes of these migrating semi-diurnal and diurnal tides to be slowly varying with altitude for $z >$ 180 km because of molecular viscosity (e.g., Roble, 1995). Additionally, tidal amplitudes of ∼150 m/s are not uncommon in the thermosphere. Therefore, the mean wind shown here is likely due to a migrating diurnal tide.

When the background winds are opposite to a GW's propagation direction, the GW's dissipation altitude in the thermosphere increases, because the GW's intrinsic frequency and vertical wavelength are much larger than when the background winds are in the direction of GW propagation or are zero (Fritts and Vadas, 2008). However, if the background winds are too strong and are opposite to a GW's propagation direction, then the GW's intrinsic frequency will equal the buoyancy frequency. At that altitude, an upward-propagating GW becomes evanescent. If the vertical extent of the wind barrier is relatively small, then the GW can tunnel through it to higher altitudes. Otherwise, the GW reflects downwards (Cowling et al., 1971; Waldock and Jones, 1984). From Fig. 8, GWs #1 and 2 were likely evanescent or nearly evanescent at $z\sim$180−200 km at the times corresponding to constant phase lines #5, 9, and 10, because λ_z was very large and

Author's personal copy

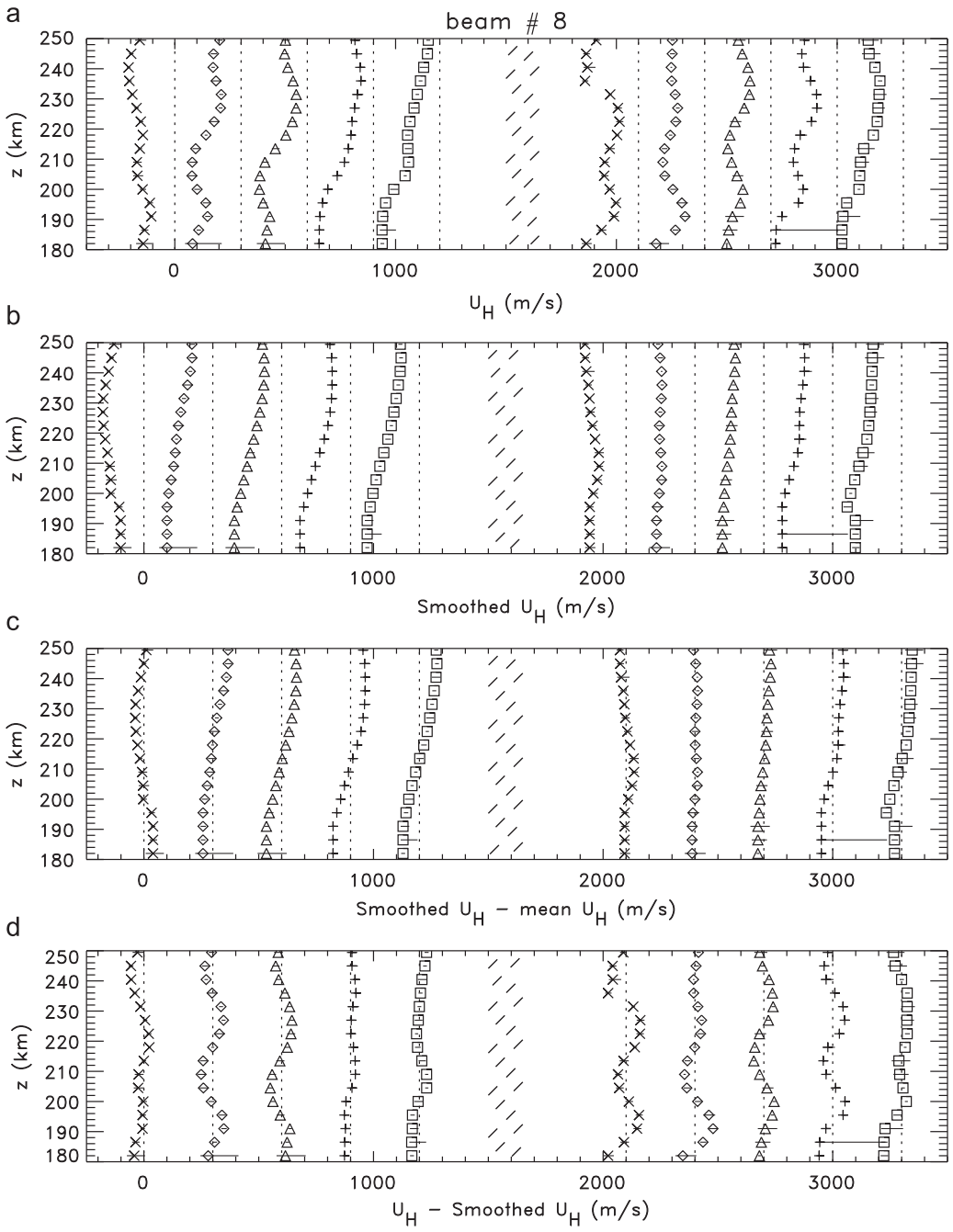

Fig. 9. (a) Extracted background, horizontal, neutral winds, U_H, for beam #8. Profiles are offsetted by 300 m/s. (b) The extracted winds from beam #8, smoothed using a nine-point running average to remove the small-scale oscillations. (c) The smoothed winds in (b) minus the average from $z = 180$ to 250 km for each phase line. (d) The extracted winds in (a) minus the smoothed winds in (b). Here, we use the same symbols for the phase lines as in Fig. 8.

$\tau_{Ir} \sim \tau_B$. However, the amplitudes of V_{los} are non-zero up to $z \sim 220-240$ km. Because V_{los} reflects the GW's velocity amplitude more accurately than $\delta N_e/\overline{N}_e$ (see Section 5), if GWs #1 and 2 were truly evanescent, then they apparently tunneled through the wind barrier to higher altitudes; if they had not tunneled, then they would have reflected downwards, and V_{los} would have been negligible for $z > 200$ km in Fig. 6.

When a GW's intrinsic period equals the buoyancy period, but the wind barrier's vertical extent is small enough to allow for GW tunneling to higher altitudes, the wind that is extracted from the dispersion relation does not equal the actual wind, but instead is smaller than the actual wind. Using Eq. (32), the strongest background wind that can be extracted from the dispersion relation when $\tau_{Ir} = \tau_B$ is

$$\max(U_H) \simeq \lambda_H \left(\frac{1}{\tau_r} - \frac{1}{\tau_B} \right). \tag{33}$$

Essentially, once a GW's phase lines are vertical because the GW encounters an oppositely directed wind barrier of amplitude $\max(U_H)$, no further steepening of the phase lines can occur if the winds increase even further. Therefore, Eq. (33) represents the largest wind that can be extracted by this method for a given GW. Using Table 1, the largest wind that can be extracted by this method for GWs #1 and 2 is

$$\max(U_H) \simeq (320-360)\,\mathrm{m/s} \tag{34}$$

Author's personal copy

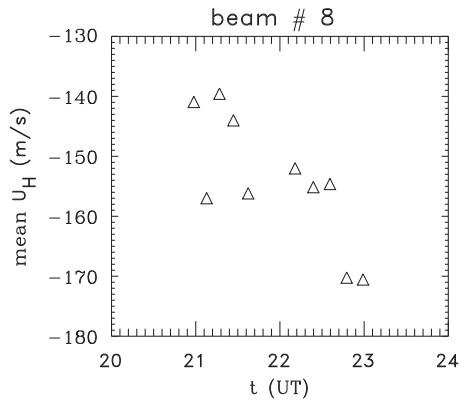

Fig. 10. Mean wind values for beam #8 as a function of the mean time (triangles). This is the average from $z = 180$ to 250 km of the smoothed winds in Fig. 9b.

for a buoyancy period of 7 min for the MSIS model at $z\sim190$ km. From Fig. 9a, the largest extracted winds at $z\sim180-200$ km are $U_H \simeq -(280-300)$ m/s. Therefore, it is possible that we are not extracting the actual wind amplitudes at these altitudes and times because of GW evanescence and tunneling. For the same ground-based period, a larger wind can be extracted from the constant phase lines of a GW with a larger horizontal wavelength, for example.

In Fig. 11a, we show the calculated background wind accelerations, $\Delta U_H(z)/\Delta t(z)$, using the extracted winds from Fig. 9a and the times from Fig. 7. Although the accelerations due to the smaller-scale oscillations are visible, the accelerations due to the slowly moving winds are also visible, with amplitudes of $\partial u'/\partial t\sim(0.05-0.1)\,\mathrm{m/s^2}$. Fig. 11b shows the calculated values of

$$|\lambda_z(dU_H/dz)/(2\pi U_H)| \tag{35}$$

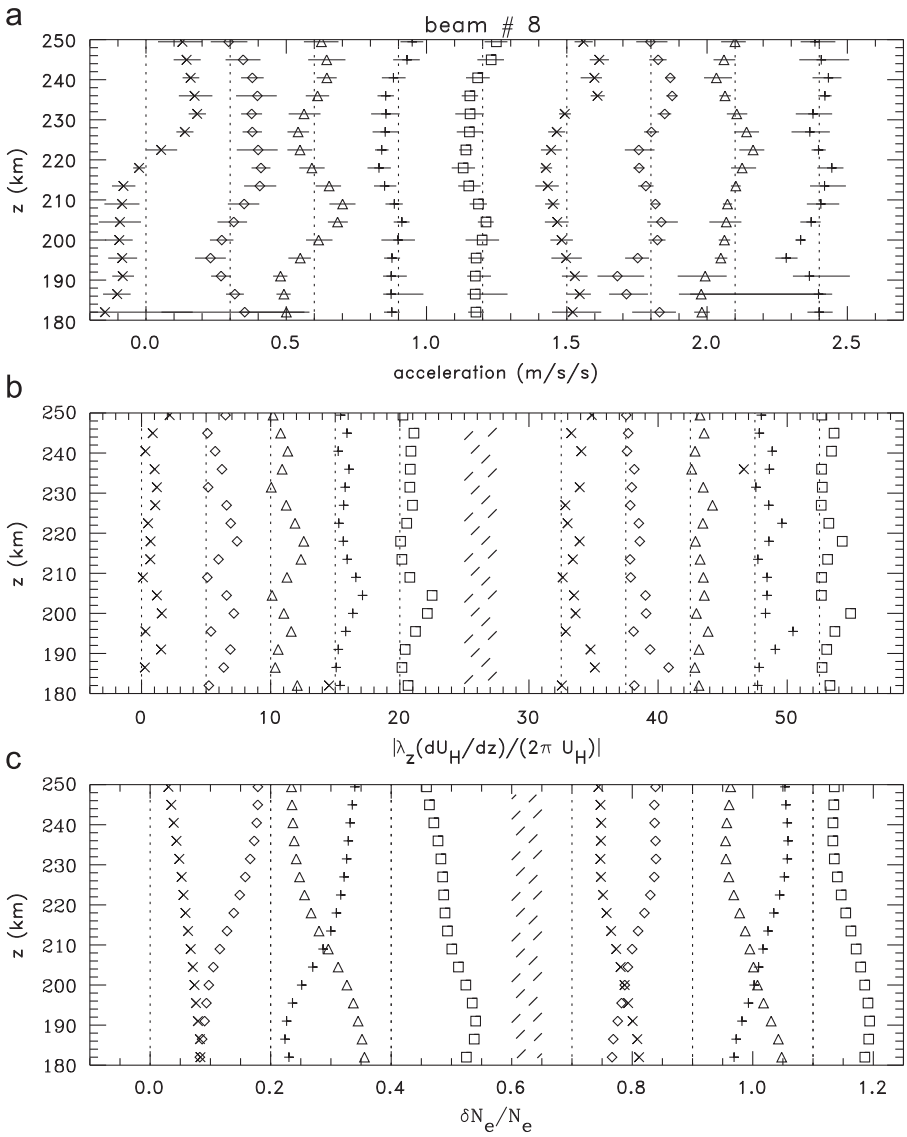

Fig. 11. (a) Neutral, background wind accelerations, $\Delta U_H/\Delta t$, using the data in Figs. 7 and 9a. The acceleration profiles between the first and second (1–2), second and third (2–3), etc., wave phases are shown as ×'s, diamonds, triangles, +'s, squares, ×'s, diamonds, triangles, and +'s, respectively. Profiles are offsetted by 0.3 m/s^2. (b) $|\lambda_z/(2\pi U_H/(dU_H/dz)|$. Profiles are offsetted by 5. (c) $\delta N_e/\overline{N}_e$ for GWs #1 and 2 along the constant wave phase lines. Odd-numbered profiles are offsetted by 0.2. The symbols in (b) and (c) are the same as in Fig. 8.

Author's personal copy

using the extracted winds from Fig. 9a. Most of the large variations occur on vertical scales of 35–40 km, which is the scale of the oscillations. According to Eq. (8), Eq. (35) must be less than one in order to ensure that the wind shear terms in the fluid equations can be neglected in deriving the GW dissipative dispersion relation. Note the important factor of 2π in the denominator; this factor arises because it is m, and not $1/\lambda_z$, which appears in the equations of motion. Although Fig. 11b (smoothed over the vertical scale of the oscillations) is often <1, it is sometimes larger than one, up to 2–3. Thus, although the calculated winds likely approximate the actual winds at most altitudes and times in beam #8, it is difficult to say how closely these calculated winds equal the actual winds when $|\lambda_z(dU_H/dz)/(2\pi U_H)|>1$. Comparison with experimentally determined wind values may shed light on the accuracy of these extracted winds when $|\lambda_z(dU_H/dz)/(2\pi U_H)|>1$.

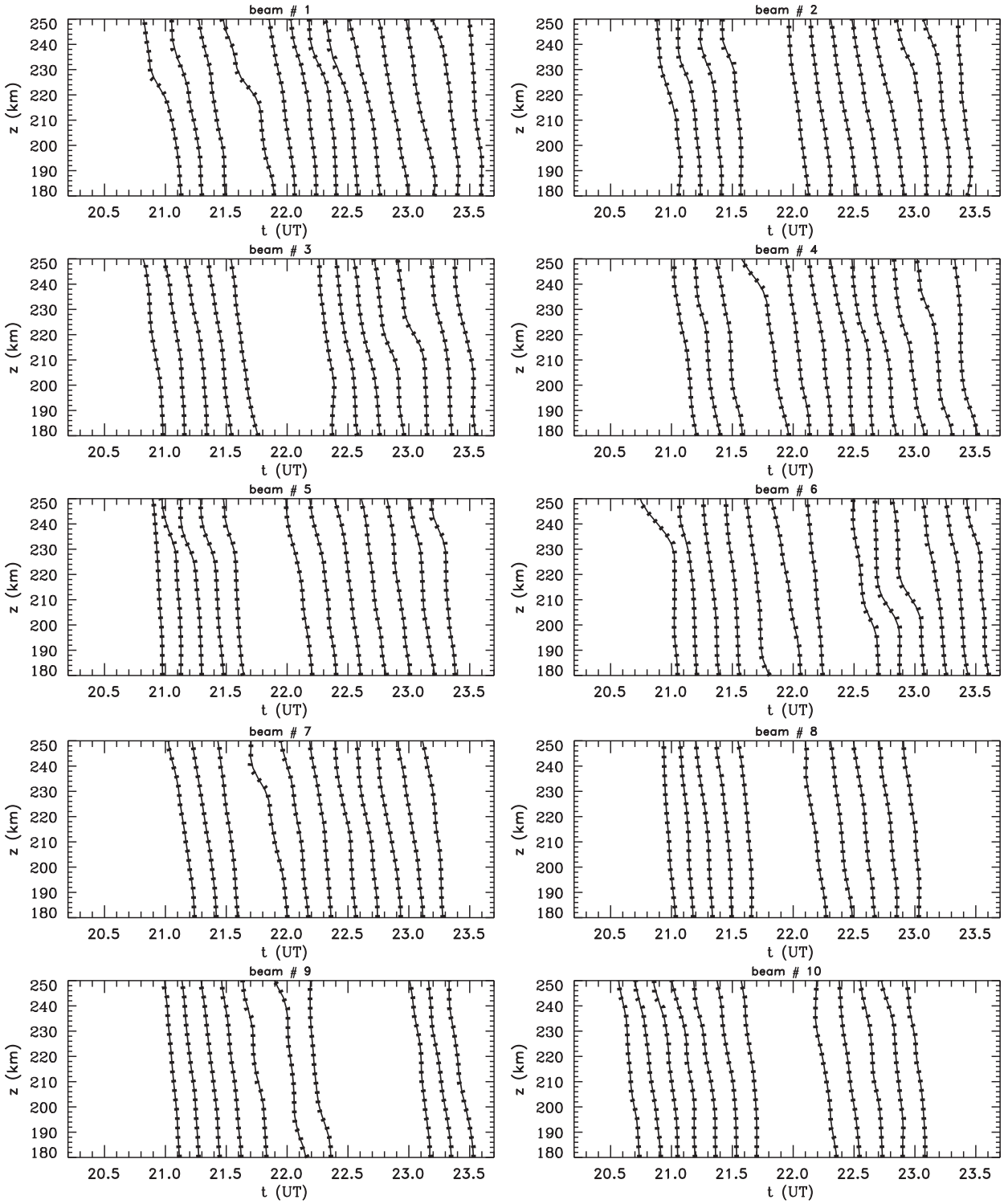

Fig. 12. Times when the GW phases are maximum as a function of altitude for all 10 beams, as labeled (dotted lines). Three-point running average of the same times (solid lines).

Author's personal copy

Fig. 11c shows $\delta N_e/\overline{N}_e$ along each constant wave phase line in Fig. 7. The overall, large, negative to positive oscillation of $\delta N_e/\overline{N}_e$ every 10–12 min is clearly visible, and is due to GWs #1 and 2. Note that the relative amplitudes of the smaller-scale oscillations are smaller here as compared to the horizontal wind amplitudes. Additionally, the slowly moving wave with the large λ_z visible in Fig. 9b and c is not clearly visible here. This is likely because w' is very small for this wave, even though u' is large (see Section 4.3). We will see in Section 5 that $\delta N_e/\overline{N}_e$ is approximately proportional to a GW's vertical velocity amplitude, w', because the magnetic field lines at PF are nearly vertical. Therefore, a small value of w' implies a small value of $\delta N_e/\overline{N}_e$.

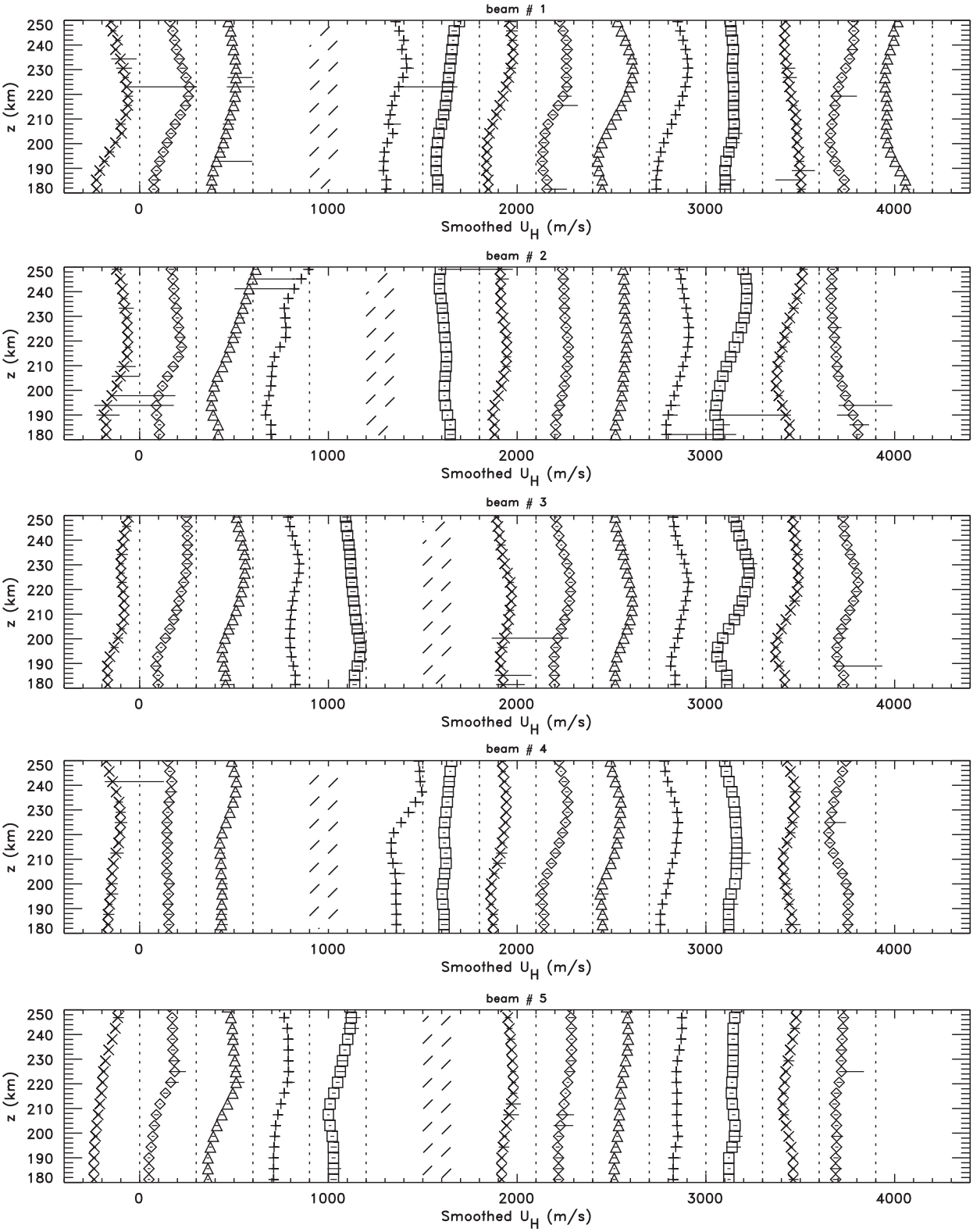

Fig. 13. Extracted background, horizontal, neutral winds, U_H, for beams #1–5, as labeled, smoothed via a nine-point running average to eliminate the small-scale oscillations on vertical scales of 35–40 km. Profiles are offsetted by 300 m/s. We use the same symbols for the phase lines as in Fig. 8.

Author's personal copy

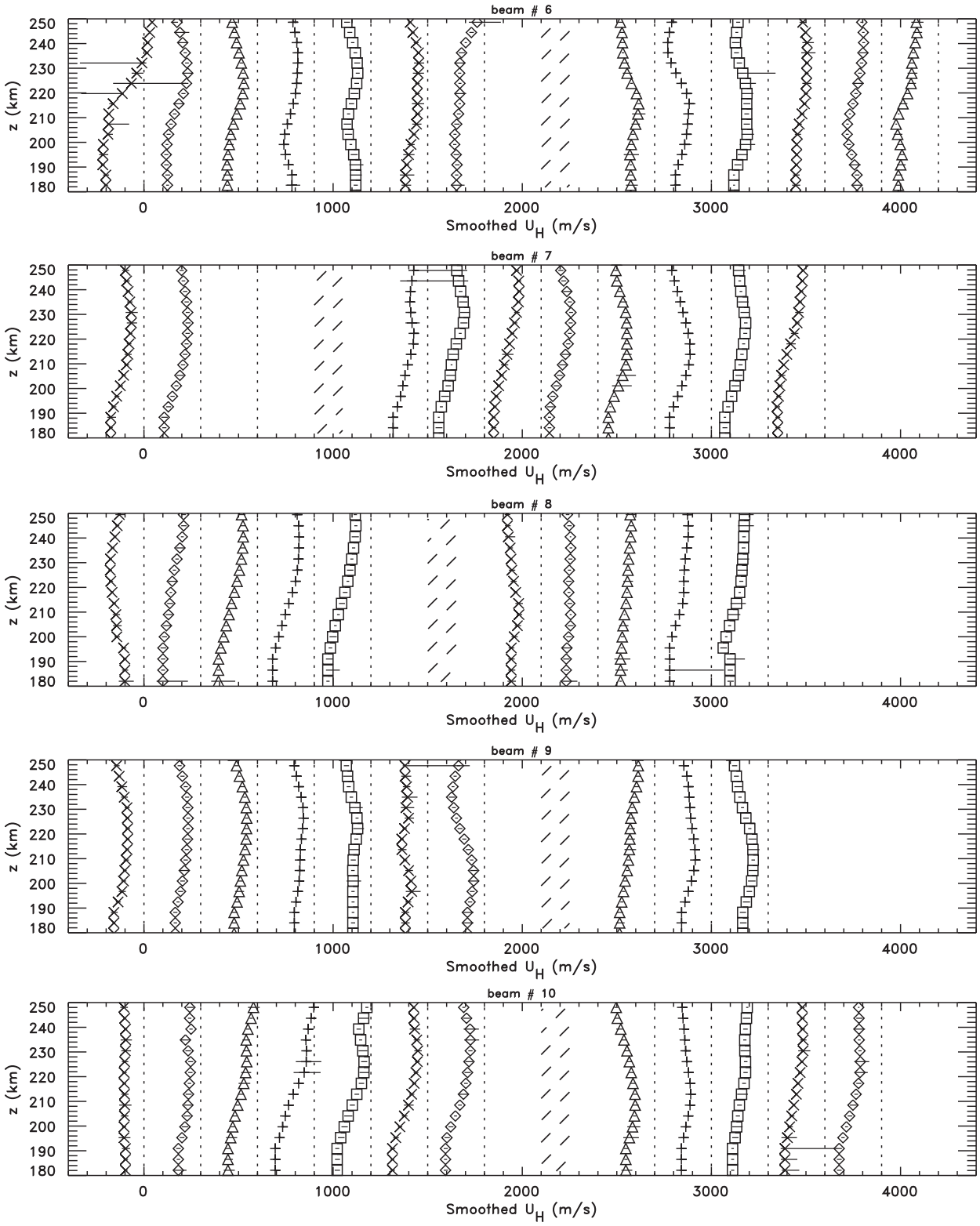

Fig. 14. Same as in Fig. 13, but for beams #6–10, as labeled.

Fig. 12 shows the times and altitudes where the wave phases of GWs #1 and 2 are maximum for all of the beams in the experiment. The dot lines are identical to the thin white lines in Fig. 2, although not all of the thin white lines in Fig. 2 are analyzed. Note that the time when GW #2 is first observed increases along any meridional direction (e.g., beams 1–3, beams 4–6, and beams 7–9), indicating a SEward propagation direction.

Figs. 13 and 14 show the extracted, smoothed horizontal, neutral winds for beams #1–5 and #6–10, respectively. Here, we have applied a nine-point running average to the extracted winds, in order to eliminate the small-scale oscillations. These phase lines correspond to the same phase lines as in Fig. 12. Figs. 13 and 14 show that there is a persistent, mean, horizontal wind to the NW with an amplitude of $U \sim -150$ m/s in all of the beams.

Author's personal copy

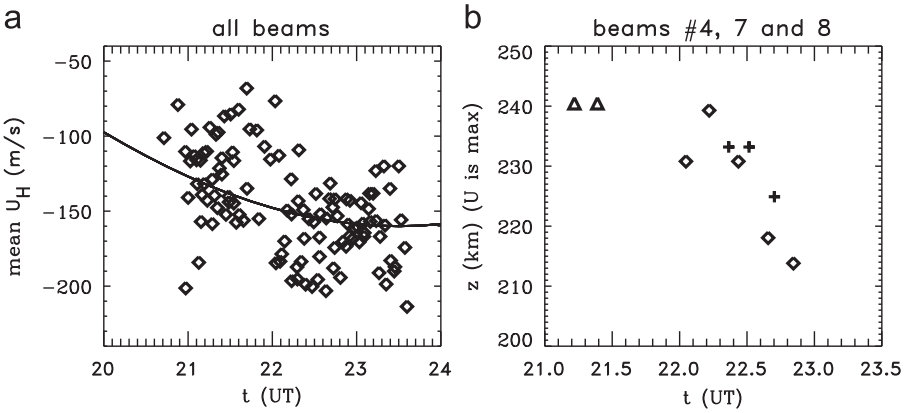

Fig. 15. (a) Mean wind values for all of the beams as a function of the mean time (diamonds). Here we average the wind for each phase line in Figs. 13 and 14 from $z = 180$ to 250 km. (b) Altitudes where the slowly moving wave is the largest as a function of time for three phase lines in beam #4 (+'s), five phase lines in beam #7 (diamonds) and two phase lines in beam #8 (triangles).

Additionally, the slowly moving, upward-propagating wave identified previously in beam #8 is visible in most of the beams, with $\lambda_z \sim 80$ km. Note that this wave is often present in adjacent beams. For example, this large-scale wave is easily seen in beam #4 at $t \sim 22.2-22.9$ UT and in beam #7 at $t \sim 22.0-23.0$ UT.

Fig. 15a shows the mean wind in all of the beams as a function of the mean time. These mean winds are obtained by averaging the smoothed winds in Figs. 13 and 14 from $z = 180$ to 250 km. We see that the mean winds in all of the beams are consistent; they are all NW with slowly changing amplitudes from 100 to 200 m/s. This consistency lends credibility to our data analysis method and dynamical inferences. Although there is more variability for all of the beams than from beam #8 only, this is to be expected from the increased number of data points. We note that the approximate error in our extracted winds is ±40 m/s. Additionally, the mean wind consistently decreases from $\overline{U_H} \sim -(80-100)$ to $-(170-180)$ m/s over the 3-h interval from 20.8 to 23.8 UT. As discussed previously, this change in the mean wind with time is likely due to the migrating diurnal tide. We overlay a wave with a 24-h period and which peaks a few hours after noon LST in Fig. 15a in order to suggest how a diurnal tide might vary with time. This figure suggests that PFISR may be able to measure portions of the diurnal tidal cycle using this extraction method.

4.3. Properties of the slowly moving wave

The smoothed, extracted winds in Figs. 13 and 14 are composed of a slowly varying mean component and a slowly moving wave with a vertical wavelength of $\lambda_z \sim 80$ km. Here, we explore this wave further.

In beams #4, 7 and 8, the slowly moving wave is easy to see and occurs over many consecutive phase lines. In Fig. 15b, we show the altitude where U_H is the largest for selected, consecutively occurring phase lines from beams #4, 7 and 8. We see that the phase of the wave descends approximately linearly in time, with a slow vertical phase velocity of $c_z \sim -(5-7)$ m/s. Since the vertical phase velocity is $c_z = \omega_r/m$, this slow phase speed is indicative of a large-scale GW or tide with observed period,

$$\tau_r = |\lambda_z|/c_z \tag{36}$$

of 3–5 h. A medium- or low-frequency GW with a period small enough to neglect the Coriolis force has a horizontal wavelength of

$$|\lambda_H| \simeq \frac{|\lambda_z|N}{\omega_{Ir}} \simeq \frac{|\lambda_z|N}{\omega_r - |k_H|U_B}, \tag{37}$$

where U_B is the projection of the background wind along the propagation direction of the GW. We can rewrite this equation as

$$|\lambda_H| \simeq \tau_r \left(\frac{|\lambda_z|N}{2\pi} + U_B \right). \tag{38}$$

If we assume this wave was propagating NWward, then using $N \sim 0.015\,\mathrm{s}^{-1}$ at $z \sim 200$ km and $U_B = 150$ m/s, then $\lambda_H \sim (6000-8000)$ km and $\tau_{Ir} \sim 9-11$ h. Using Eq. (10), this wave's dissipation altitude would then be $z_{\mathrm{diss}} \sim 170-180$ km, which is likely too low to explain this wave's amplitude profile, since a wave's amplitude is negligible several density scale heights above its dissipation altitude (Vadas, 2007). Instead, if this wave was propagating SEward, then $\lambda_H \sim (700-900)$ km and $\tau_{Ir} \sim 1-1.5$ h. Using Eq. (10), this wave would dissipate at $z_{\mathrm{diss}} \sim 220-225$ km, which is more compatible with the wind amplitudes. Since we do not know this wave's propagation direction, we estimate that this slowly moving wave has a large horizontal wavelength of $\lambda_H \sim 700-8000$ km.

Because this wave's horizontal velocity amplitude is large, it is a major component of the background, thermospheric winds through which the GWs propagate. This 3–5 h wave has a negative peak at $z \sim 190$ km and a positive peak at $z \sim 230$ km, and has a horizontal wind amplitude of $u' \sim 50-75$ m/s. At $z \sim 180-200$ km, it increases the background winds, while at $z \sim 230$ km, it decreases the background winds. This leads to a total background wind in the NW direction of $\sim -(150-250)$ m/s at $z \sim 180-200$ km and $\sim -(75-150)$ m/s at $z \sim 230-250$ km. This slowly moving wave therefore caused the horizontal wind amplitudes to decrease approximately linearly with altitude, as was noted in Fig. 9b and c.

Finally, although this wave's horizontal velocity amplitude was very large, $|u'| \sim 50-75$ m/s, it vertical velocity amplitude was small. Using the anelastic continuity equation, this GW's vertical velocity perturbation was

$$w' \sim \frac{\lambda_z u'}{\lambda_H} \tag{39}$$

which is as large as $w' \sim 1$ and 9 m/s if this wave was propagating NW and SE, respectively.

4.4. Acceleration of the background wind

Now that we have discussed how the background winds are modulated by the presence of a large-scale, slowly moving wave, we investigate the neutral, dynamical processes which occur on much shorter time scales, ~30–90 min. In Fig. 16, we show the

Author's personal copy

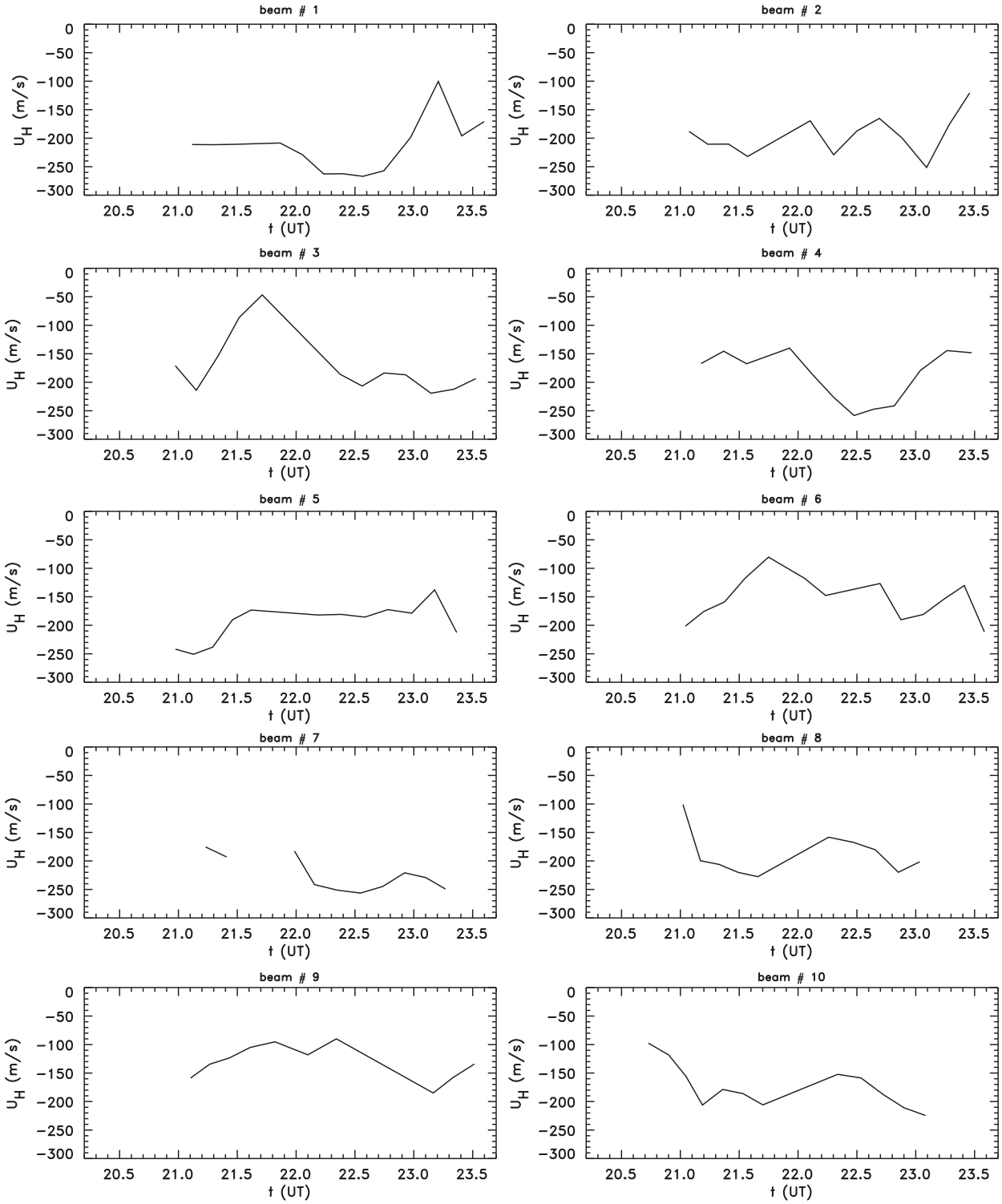

Fig. 16. The extracted, smoothed winds from Figs. 13 to 14 for all 10 beams at $z\sim187$ km as solid lines.

smoothed horizontal winds as a function of time at $z\sim190$ km. Note that at these altitudes, $\delta N_e/\overline{N}_e$ is large; therefore the determination of λ_z and the background winds from the constant wave phase slopes are likely reasonably accurate. At much higher altitudes, $\delta N_e/\overline{N}_e$ is smaller, and can decrease rapidly to zero for some of the phase lines above $z>210$ km, thereby making the extracted winds at these higher altitudes somewhat less certain. We see that the winds are to the NW in every beam. In some of the beams, the extracted winds are fairly constant with time, e.g., beams #7 and 9. In other beams, however, the background winds vary rapidly in time. In beams #3 and 6, which are adjacent beams (see Fig. 2) the winds are large and negative initially, decrease rapidly by $\sim125-150$ m/s in the SE direction over 30–40 min, then increase to their initial large/negative values over 50–80 min. These accelerations happen at nearly the same time, with the peak changes in the velocities occurring at $t\sim21.2-21.7$ UT. In beams #1, 2, and 4, there is also a large SE acceleration in the background winds at $t\sim22.8-23.5$ UT. These accelerations are

Author's personal copy

also rapid, occurring over 25–30 min, with final wind changes of ~100−150 m/s. The largest SEward accelerations have amplitudes of $\partial u'/\partial t \sim 0.1\,\mathrm{m/s^2}$. In comparison, the acceleration of GW #1 or 2 at this altitude is much smaller: $\partial u'/\partial t \sim (10\,\mathrm{m/s})/(20\,\mathrm{min}) \sim 0.01\,\mathrm{m/s^2}$. It is also important to notice that the extracted winds in beams #8 and 10 stop suddenly at $t = 23.0$ UT. Examination of Fig. 2 shows that GW #2 disappears at this time in these beams. This occurs at the same time when a strong SE acceleration of the horizontal winds is occurring in beams #1, 2, and 4. Because GWs #1 and 2 are propagating SEward, they need to propagate through beams #1, 2, and 4 before arriving in beams #8 and 10 (see Fig. 2). Therefore, something suddenly blocked their propagation at $t \sim 23.0$ UT. We will discuss a possible cause in Section 6.

Finally, the beams in this experiment are equally gridded in the geomagnetic zonal and meridional directions, with horizontal distances between the beams in the thermosphere of ~50 km. Since these large SEward accelerations occur in some beams but not in other beams at the same time, these accelerations were therefore spatially inhomogeneous in the horizontal direction on scales of order 50−100 km.

It is easy to explain why the neutral winds relax back to their large/negative values in ~50−80 min after a SE acceleration ceases to occur; namely, viscosity is very large in the thermosphere (see Section 6.3). However, it is more difficult to explain the origin of the large SEward accelerations. We will argue in Section 6.2 that these SEward accelerations may be due to the dissipation of SEward-propagating GWs that are excited by the same process which excited GWs #1 and 2, and that these SEward-propagating GWs are secondary GWs excited by the breaking of mountain waves near the mesopause.

5. GW amplitude and approximate plasma response

Although the GW dissipative dispersion relation, Eq. (1), can be used iteratively to calculate the winds as a function of altitude (see Section 4), it cannot be used to calculate the amplitude of a GW as a function of altitude. On the other hand, ray tracing can be used to determine the amplitude of a GW as a function of altitude. We have ray-traced GWs #1 and 2 through the extracted, neutral, background winds shown in Fig. 9a for beam #8. The resulting ray-traced $\lambda_z(z)$ profiles are shown in Fig. 17 for all 10 phase lines (solid lines), along with the experimentally determined values. We see that ray tracing accurately reproduces the observed values of λ_z, cutting through most of the data points. Because the ray-trace code also solves the dispersion relation Eq. (1), Fig. 17 is essentially a check that the extracted wind solutions shown in Fig. 9a are accurate. Note that there are small discrepancies in Fig. 17. These discrepancies are located where λ_z changes rapidly with altitude, and occur because we extract these winds using the λ_z profiles with a three-point running average, whereas Fig. 17 shows the experimentally determined λ_z profiles.

Ray tracing also determines the GW's momentum flux as a function of altitude, up to an unknown constant factor a which multiplies the GW's amplitude. This factor accounts for the unknown source and initial amplitude of the GW. In a manner similar to Hines (1968), for each of the wave's constant phase lines, we calculate the GW momentum flux, horizontal velocity, and vertical velocity as

$$-a(|\widetilde{u_{H0}}\widetilde{w}_0^*|^2)^{1/4}\cos^2(\omega_r t - \int m\,dz + \beta), \tag{40}$$

$$-a(|\widetilde{u_{H0}}\widetilde{u_{H0}^*}|^2)^{1/4}\cos(\omega_r t - \int m\,dz + \beta), \tag{41}$$

$$a(|\widetilde{w}_0\widetilde{w}_0^*|^2)^{1/4}\cos(\omega_r t - \int m\,dz + \beta), \tag{42}$$

respectively, where β is the phase offset, and where we have assumed that no wave reflection has occurred. If partial wave reflection occurs (as is expected, since these waves are close to evanescence and the wind shears are large at $z \sim 180-200$ km), the amplitudes will be smaller for $z > 200$ km. We transition from one phase line to the next where the phases are $\pm\pi/2$, half-way between the wave maxima and minima. Contours of the horizontal flux of vertical momentum are shown in Fig. 18a for GWs #1 and 2 using Eq. (40). Here, a was chosen so that the theoretical results roughly agree with the ion velocity and electron density measurements (see below). We see that the momentum fluxes peak at altitudes of $z \sim 220-250$ km. Additionally, the momentum flux profile is different for each phase line, and clearly depends on the background wind. For example, the momentum fluxes peak at the highest altitudes for phase lines #1, 2, 6, and 7. For these phase lines, the winds are larger to the NW for $z > 235$ km (see Fig. 9a), which leads to higher penetration altitudes prior to wave dissipation.

Contours of the horizontal and vertical velocity perturbations are shown in Fig. 18b and c, respectively, using Eqs. (14), (15), (41), and (42). We note that the GW's horizontal and vertical velocity perturbations generally peak at similar altitudes. When $u'_H \sim w'$, this is an indication that the wave intrinsic frequency is nearly equal to the buoyancy frequency. Note also that the GW's horizontal and vertical velocity perturbations maximize at much higher altitudes, i.e., $z \sim 210-250$ km, than $\delta N_e/\overline{N}_e$ (see Fig. 2).

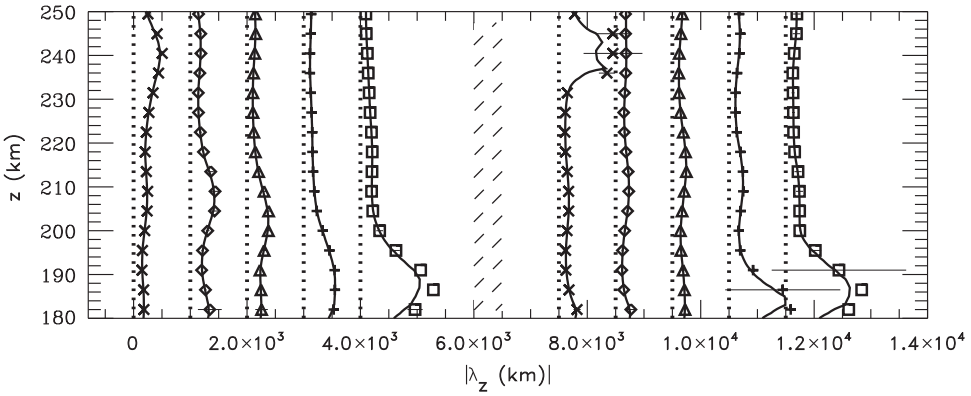

Fig. 17. All 10 $|\lambda_z(z)|$ profiles obtained by ray-tracing GWs #1 and 2 through the extracted winds in Fig. 9a from beam #8 (solid lines). Profiles are offsetted by 1000 km. As before, GWs #1 and 2 are separated by a hatched region. The dot lines show $\lambda_z = 0$ for each constant phase line. We use the same symbols for the phase lines as in Fig. 8.

Author's personal copy

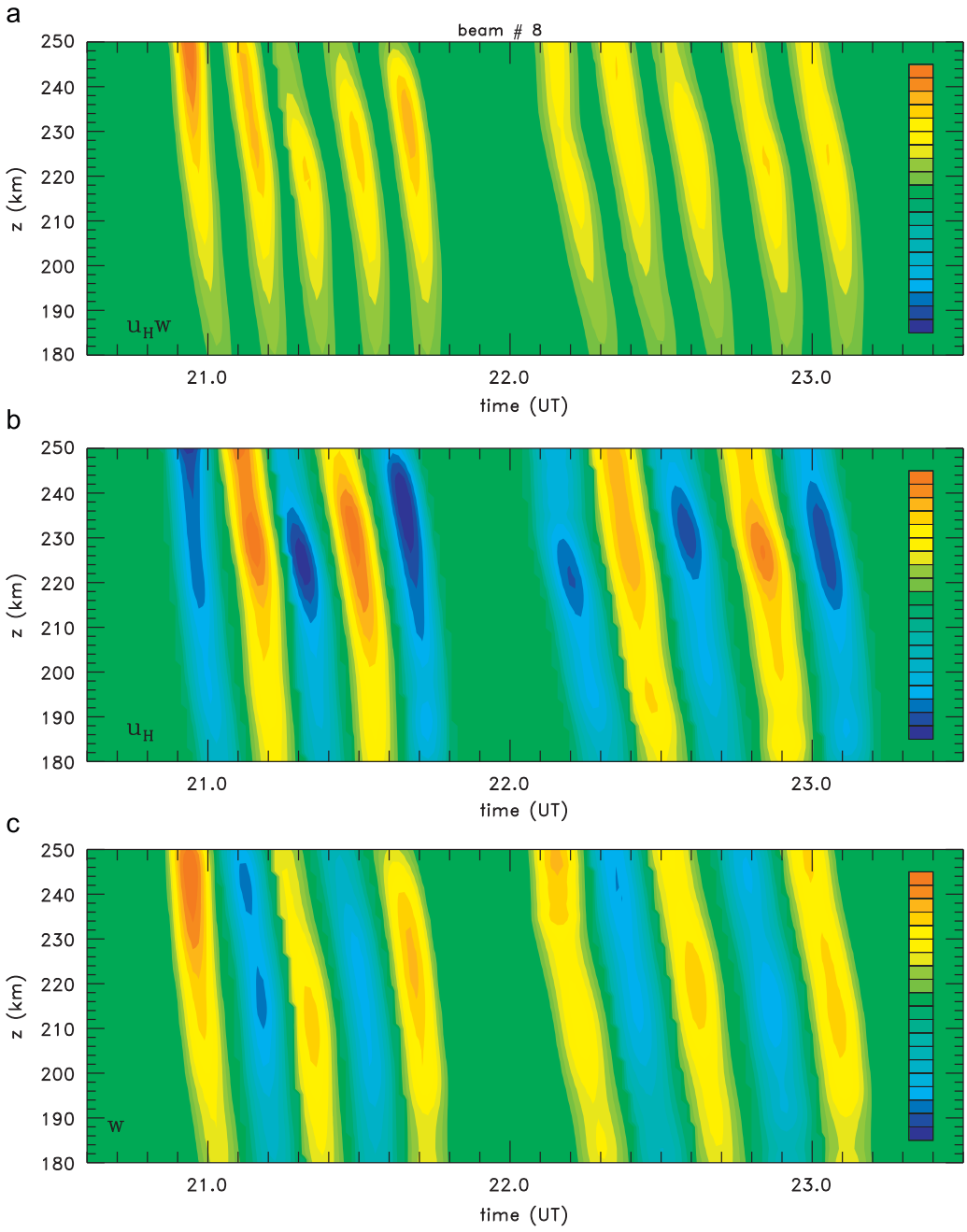

Fig. 18. (a) Contours of GW horizontal flux of vertical momentum. The maximum value on the color scale is $\pm 1600\,m^2/s^2$. (b) Contours of horizontal velocity using Eq. (14). The maximum value is 47 m/s. (c) Contours of vertical velocity using Eq. (15). The maximum value on the color scale is ± 40 m/s. All contours are shown in intervals 10% of their maximum values. The color bar at the far right side of each plot shows the maximum (top) and minimum (bottom) colors used for these 10% intervals.

To estimate the plasma response to this GW, the ion continuity and momentum equations need to be solved with the appropriate drag, heating, and cooling processes taken into account. Since we only seek an approximate solution, we first assume that O^+ is the dominant ion in the region of interest. This assumption is quite accurate above $z\sim 200$ km. The electron continuity equation is then (e.g., Schunk and Nagy, 2000)

$$\partial N_e/\partial t + \nabla.(N_e \mathbf{v}_{O^+}) = Q - L, \tag{43}$$

where N_e is the electron density, $\mathbf{v}_{O^+}$ is the ion velocity in the direction of the magnetic field, Q is a production term, and L is a loss term. Here, we have neglected drag, friction and other coupling processes which may be important when assessing the full impact of a GW on the plasma (Kirchengast et al., 1996). We assume that the ion velocity roughly equals the component of the GW velocity parallel to the magnetic field.

At PF, the magnetic field is nearly vertical, with a magnetic dip angle of $I = 77.5^\circ$ and an angle clockwise from north of $\zeta = -154.3^\circ$. The unit vector pointing along the direction of the magnetic field (which is the same as the direction of beam #10) is given by Eq. (25), i.e., $\mathbf{A_B}$, where $\theta = 77.5^\circ$ and $\zeta = -154.3^\circ$. We assume that the GW's amplitude is linear, and write the perturbation velocity vector as

$$\begin{aligned}\mathbf{v}' &= u'\hat{\mathbf{i}} + v'\hat{\mathbf{j}} + w'\hat{\mathbf{k}} \\ &= (u'_0\hat{\mathbf{i}} + v'_0\hat{\mathbf{j}} + w'_0\hat{\mathbf{k}})\exp(i\{kx + ly + mz - \omega_r t\}) \\ &= (u'_0\hat{\mathbf{i}} + v'_0\hat{\mathbf{j}} + w'_0\hat{\mathbf{k}})\exp(i\phi),\end{aligned} \tag{44}$$

Author's personal copy

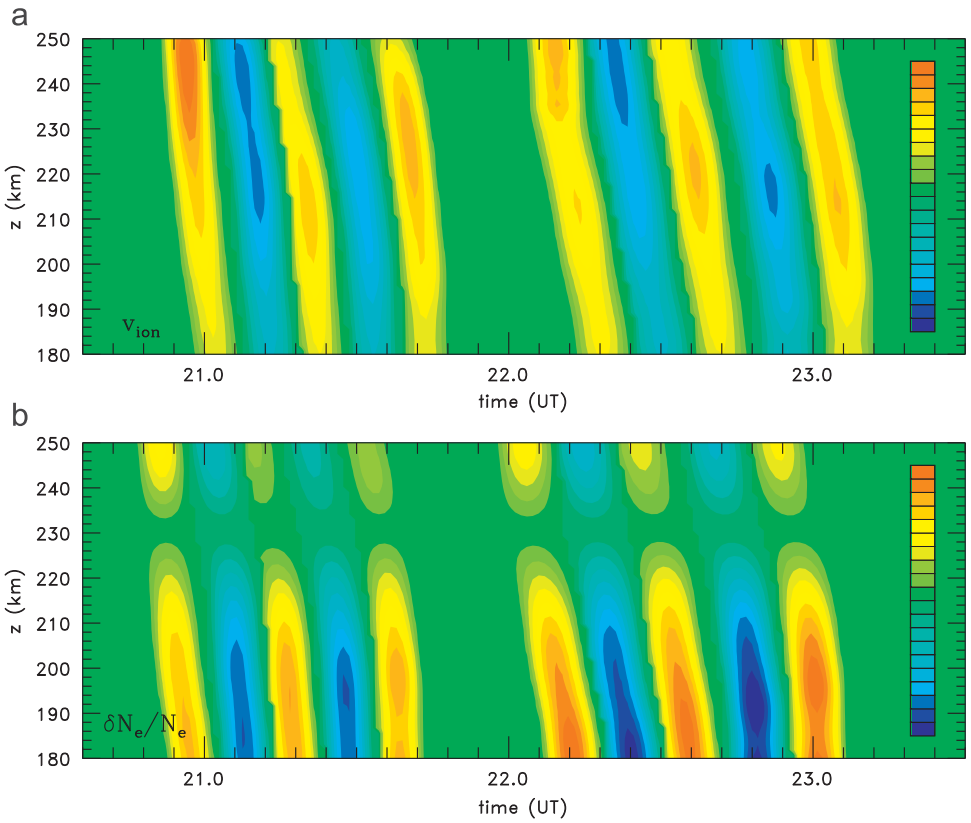

Fig. 19. (a) Contours of the calculated ion velocities using Eq. (45). The maximum value on the color scale is ±42 m/s. (b) Contours of the calculated relative electron density perturbation, $\delta N_e/\overline{N}_e$, using Eq. (51). The maximum value on the color scale is ±0.1. All contours are shown in intervals 10% of their maximum values. The color bar at the far right side of each plot shows the maximum (top) and minimum (bottom) colors used for these 10% intervals.

where u'_0, v'_0, and w'_0 are the zonal, meridional and vertical velocity amplitudes of the GW (i.e., along a constant wave phase line). Additionally, the wave phase is ϕ from Eq. (23). The plasma response is also linear with our assumptions. The component of the GW perturbation velocity along the direction of the magnetic field is then

$$v_{O^+} = \mathbf{v}'.\mathbf{A_B} = [\cos\theta(u'_0\sin\zeta + v'_0\cos\zeta) + w'_0\sin\theta]\exp(i\phi) \quad (45)$$

$$= [u'_{H_0}\cos\theta\cos(\zeta-\psi) + w'_0\sin\theta]\exp(i\phi), \quad (46)$$

where $u' = u'_H\cos(90-\psi) = u'_H\sin\psi$ and $v' = u'_H\sin(90-\psi) = u'_H\cos\psi$. The perturbation ion velocity vector is then

$$\mathbf{v}_{O^+} = v_{O^+}\mathbf{A_B} = v_{O^+0}(\cos\theta\sin\zeta\hat{\mathbf{i}} + \cos\theta\cos\zeta\hat{\mathbf{j}} + \sin\theta\hat{\mathbf{k}})\exp(i\phi), \quad (47)$$

where v_{O^+0} is the ion amplitude along a constant wave phase line. Fig. 19a shows contours of the modeled ion velocity, $\mathbf{v}_{O^+}$, using Eq. (47). We see that the ion velocity peaks at $z\sim210-250$ km, above the altitude where $\delta N_e/\overline{N}_e$ peaks, as has been noted previously (Kirchengast et al., 1996). Additionally, Fig. 19a very similar to the vertical velocity contours in Fig. 18c, because the magnetic field lines at PFISR are nearly vertical. Although the ion velocity data shown in Fig. 6 are not very accurate, we can still use it for comparison purposes, especially at 180 km $< z <$ 250 km. We see that in general, the ion velocities peak at altitudes of $z\sim220-250$, which agrees qualitatively with Fig. 19a. Note that the peak values for the majority of the phase lines in beam #8 are 20–30 m/s, consistent with Fig. 6.

We can also estimate the electron density perturbations that result from this GW using this simple, single-ion model. Because the magnetic field line is not parallel to the direction of GW propagation, the effective horizontal wavelength along the magnetic field line, λ_B, is larger than the GW's horizontal wavelength:

$$\lambda_B = \frac{\lambda_H}{\cos(\zeta-\psi)}. \quad (48)$$

Because the angle between the magnetic field line and GWs #1 and 2 is 64 and 53°, $\lambda_B = 495$ and 340 km, respectively. We can rewrite the ion velocity perturbation as

$$\mathbf{v}_{O^+} = v_{O^+0}(\cos\theta\hat{\mathbf{i}}_H + \sin\theta\hat{\mathbf{k}})\exp(i(k_Bx_B + mz - \omega_r t)), \quad (49)$$

where $k_B = 2\pi/\lambda_B$, $\hat{\mathbf{i}}_H = (\sin\zeta\hat{\mathbf{i}} + \cos\zeta\hat{\mathbf{j}})$ is the unit vector of the projection of the magnetic field onto the horizontal plane in geographic coordinates, x_B is the length in this projected horizontal plane, and $k_Bx_B = kx + ly$. The total electron density then is a mean background component plus an oscillatory component:

$$N_e = \overline{N}_e + \delta N_e\exp(i(k_Bx_B + mz - \omega_r t)) = \overline{N}_e + \delta N_e\exp(i\phi). \quad (50)$$

Note that $\delta N_e/\overline{N}_e$ has the same wave phase as the GW, up to factors of ±1 or ±i. Eq. (50) shows that assuming a single-ion species and neglecting chemical and drag processes, the phase ϕ of the created electron density perturbations is the same as that for the GW (with the exception of a constant phase shift). Note that this assumption allowed us to approximate the λ_z profiles determined from the electron density perturbations as being the same as the λ_z profiles for the GW in Section 3. We note that this approximation is best for $z\gtrsim200$ km, where our assumptions are most applicable.

Plugging Eqs. (49) and (50) into Eq. (43), neglecting the production and loss terms, and linearizing, the relative electron

Author's personal copy

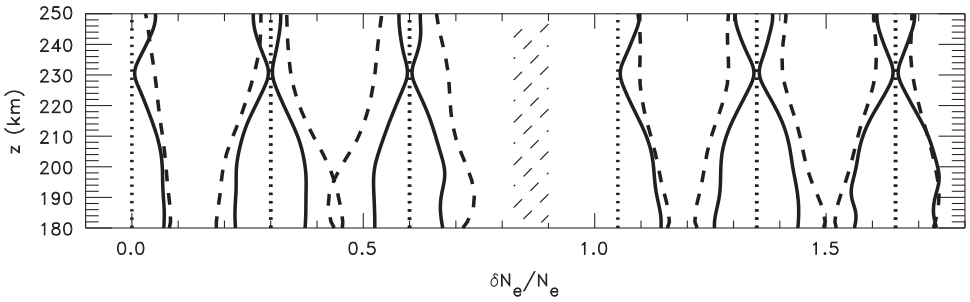

Fig. 20. $\delta N_e/\overline{N}_e$ from a simple, single-ion model using Eq. (51) (solid line) and from the data (dash line).

density perturbation is

$$\frac{\delta N_e}{\overline{N}_e} \simeq -\frac{i\sin\theta v_{O^+0}}{\omega_r}\left(\frac{1}{\overline{N}_e}\frac{d\overline{N}_e}{dz}\right) + \frac{1}{\omega_r}\left[(k_B\cos\theta + m\sin\theta)v_{O^+0} - i\sin\theta\frac{dv_{O^+0}}{dz}\right]. \quad (51)$$

The terms in the square bracket on the RHS of Eq. (51) are the divergence of the ion velocity, $\nabla.\mathbf{v}_{O^+}$. This term is small if the fluid moves a distance vertically which is much less than the density scale height. In this case, the vertical distance the neutral fluid moves from GWs #1 and 2 is $\Delta z \sim w'\tau_r/4 \sim (20\,\mathrm{m/s})(24\,\mathrm{min})/4 \sim 7\,\mathrm{km}$, which is much less than the density scale height. Therefore, we can set $\boldsymbol{\nabla}.\mathbf{v}_{O^+} \simeq 0$ here. Although the magnitude of $\delta N_e/\overline{N}_e$ is approximately proportional to the amplitude of the GW's vertical velocity, $\delta N_e/\overline{N}_e$ depends primarily on where the background electron density $\overline{N}_e$ increases/decreases rapidly with altitude.

By assuming that advection is more important than chemical and drag effects, we see that the ion velocity lags 90° behind the electron density perturbation. Using $-i = \exp(-i\pi/2)$ and Eq. (51), Eq. (50) becomes

$$\frac{N_e}{\overline{N}_e} \sim 1 + \frac{\sin\theta v_{O^+0}}{\omega_r}\left(\frac{1}{\overline{N}_e}\frac{d\overline{N}_e}{dz}\right)\exp[i(k_B x_B + mz - [\omega_r t + \pi/2])]. \quad (52)$$

Therefore, for fixed x_B and z, the wave phase for the electron density perturbation, $\omega_r t' + \pi/2$, is the same as the wave phase for the ion velocity, $\omega_r t$, at $t' = t - \pi/2\omega_r$, which is a quarter of a wave period earlier than for the ion velocity when advection is the only important effect.

Fig. 19b shows contours of the electron density perturbation, $\delta N_e/\overline{N}_e$, using Eq. (51) with $\nabla.\mathbf{v}_{O^+} = 0$. We see that $\delta N_e/\overline{N}_e$ peaks at $z \sim 180-200$ km, in rough agreement with Fig. 2. Note that this peak occurs where $\overline{N}_e$ increases rapidly with altitude at the bottomside of the F region. Fig. 20 compares the theoretical calculation of $\delta N_e/\overline{N}_e$ with the data. We see that this simple theory, especially the shape of the curves, agrees reasonably well with the measured data. However, the theoretical amplitudes are up to 50% smaller for some of the phase lines at the lowest altitudes. (Note that increasing the scaling factor & by 50% would make theory agree better in Fig. 20, but the theoretical ion velocities would then be 50% too large in Fig. 19a.) The discrepancy between theory and experiment may be due to the neglection of ions other than O^+ (important for $z < 200$ km), drag, chemical and other processes in the electron density response. There are also uncertainties in the magnitude of the measured $\delta N_e/\overline{N}_e$ and V_{los}.

6. Proposed source of the GWs and SEward accelerations

In this section, we describe a possible source for GWs #1 and 2. We show how these GWs, in part, may have helped to create the SEward accelerations of the neutral winds observed in beams #1, 2, 3, 4 and 6. We also explain how these SEward accelerations may have caused the disappearance of GW #2 for $t > 23.0$ UT in beams #8 and 10.

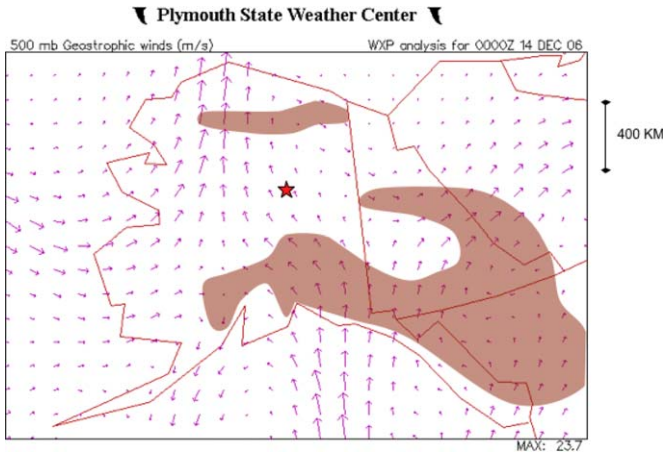

Fig. 21. Wind vectors over Alaska at 0 UT on December 14, 2006 (purple arrows). Length of vectors is proportional to the speed, which has a maximum value of 24 m/s. PFISR is shown as a red star. Areas with large mountains taller than ~2000–3000 m are shown as brown shading. (For interpretation of the references to color in this figure legend, the reader is referred to the web version of this article.)

6.1. Lower atmospheric source of GWs

GWs #1 and 2 likely originated in the lower atmosphere, because they had medium-scale horizontal wavelengths and horizontal phase speeds less than ~160 m/s. At the time of these observations, it was very cold in PF, Alaska, and no convection was occurring. There was, however, winds blowing over nearby, tall mountains in Alaska. Fig. 21 shows vectors of the winds at 500 mb (at approximately 5000 m or ~16400 ft) over Alaska just at the end of this data window, at 00:00 UT on 14 December 2006. The length of the vectors indicates the amplitude of the horizontal winds, with the maximum for this time of 24 m/s. PFISR is indicated by the red star. This figure shows a northward flow over north-central Alaska, ahead of a storm over the northern Bering Sea. The strongest winds were between balloon observations at Fairbanks (just south of PFISR) and stations on the Bering coast; this is consistent with accelerations within the confluent flow ahead of the storm. The storm was drifting slowly eastward, but had not moved much in the previous 12 h, and the 500 mb winds over northern Alaska remained fairly constant through this period (Pete Stamus, personal communication).

Fig. 21 also shows a rough sketch of the mountains taller than ~2000–3000 m as brown shading. (Note that there are many

Author's personal copy

mountains taller than 4000 m in these shaded areas.) We see that the winds are northward over the mountains 400 km to the NW of PFISR, and are NWward and northward over the mountains 400 km to the south and SE of PFISR, respectively. The region with strong winds to the NW of PFISR is approximately $30-40^\circ$ counterclockwise of north from PFISR. Since the tallest mountains are at least 12,000 ft, we estimate that the non-dimensional mountain height hN/U is about 3.0, a value that can be associated with significant mountain-wave generation (Dave Broutman, personal communication). The horizontal scales of these waves require $k<N/U=0.0008\,\mathrm{m}^{-1}$, or $\lambda_H\sim10$ km.

Mountain waves were therefore likely excited from wind flow over those mountains to the NW, south, and SE of PFISR. Since mountain waves have ~0 phase speeds, they propagate nearly straight upwards into the mesosphere, where they become nonlinear and break (Fritts and Alexander, 2003). After breaking and depositing momentum over scales of 20–30 km, we hypothesize that they excited larger-scale, high-frequency, secondary GWs via the horizontal forcing mechanism described in Vadas et al. (2003). These secondary GWs would have had $\lambda_H\sim10-600$ and $\tau_{Ir}\sim7-60$ min, and would have been excited preferentially in and against the direction of the breaking waves. But because the extracted neutral winds in the thermosphere are strong and to the NW, as determined in Section 4, only those GWs propagating nearly opposite to the background winds, or SEward, would have survived to altitudes of $z\sim200$ km. Thus, those secondary GWs excited from breaking mountain waves to the NW, but not to the S or SE, of PFISR would have been able to propagate to $z\sim220$ km at PFISR.

As further "proof" of this hypothesis, we now show that any GW excited at $z\sim80$ km over the mountains NW of PFISR must have had a wave period of ~21 min to propagate to the F region directly above PFISR. Fig. 22 shows a sketch of this proposed mechanism. We see mountain waves being excited from the northward wind V in the lower left portion of the figure. These waves travel upwards and break at $z\sim80$ km. The yellow shaded region shows the region which is horizontally accelerated because of mountain wave breaking. The purple and blue dotted lines show some of the secondary GWs which are excited by this horizontal forcing. Those excited GWs which propagate to the thermosphere above PFISR propagate along the blue dotted line. The angle between this wave breaking region and the region at $z=220$ km above PFISR is $\theta=\tan^{-1}(140\,\mathrm{km}/400\,\mathrm{km})=19^\circ$. Since a GW's frequency is related to its propagation angle and the buoyancy period via $\omega/N=\sin\theta$ (e.g., Kundu, 1990) (neglecting background horizontal winds), only GWs with ground-based periods of

$$\tau_r=\frac{\tau_B}{\sin\theta} \tag{53}$$

can travel along the dark blue dotted line and intersect the PFISR beams at $z\sim220$ km. Using an average buoyancy frequency of $N=0.015$ rad/s and $\theta=19^\circ$, any GW propagating along this line must have a ground-based period of 21 min. This is in good agreement with the periods of GWs #1 and 2.

6.2. Thermospheric body forces from dissipating GWs

GWs transport momentum; when they dissipate in the thermosphere, they transfer that momentum to the background, neutral fluid, thereby accelerating that flow (e.g., Hines and Hooke, 1972). The vertical divergence of the average momentum flux of the primary wave describes the horizontal acceleration of the fluid:

$$D_F(\mathbf{x},t)=-(1/\overline{\rho})\partial(\overline{\rho}\overline{u'w'})/\partial z. \tag{54}$$

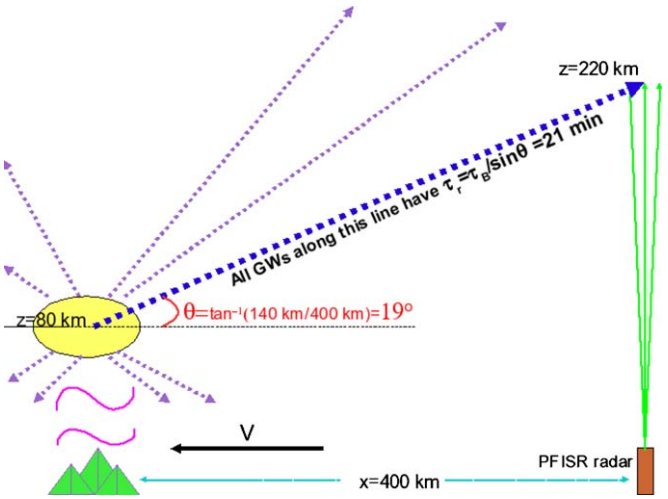

Fig. 22. Schematic showing the location of the PSISR (lower right-hand corner) and the mountains to the NW of PFISR. Mountain wave generation and breaking is shown, along with the excitation of secondary GWs which travel along the dark blue dot lines to the F region over PFISR. All GWs propagating along this dark blue dot line have ground-based periods of ~21 min, neglecting winds. (For interpretation of the references to color in this figure legend, the reader is referred to the web version of this article.)

VF2006 showed that when GWs from a convective plume dissipate in the thermosphere, they create a horizontal body force in the direction they are propagating prior to dissipating. They showed that even a small neutral wind shear of ~30 m/s in the lower atmosphere is large enough to create an asymmetry in the GW spectrum that results in a thermospheric body force. They found that this body force peaks at $z\sim180-190$ km, and that this acceleration is rapid, occurring over time scales of ~30 min. It is also known that a white noise spectrum of GWs from the lower atmosphere dissipates at $z\sim125-250$ km (Vadas, 2007). Finally, only those GWs with horizontal wavelengths $\lambda_H>100$ km and sufficiently large vertical wavelengths can propagate to the bottomside of the F layer prior to dissipating (Vadas, 2007; Fritts and Vadas, 2008). Because the horizontal and vertical scales of the secondary GWs are similar to those excited from the convective plume studied in VF2006, it is likely that a spectrum of secondary GWs excited by breaking mountain waves creates a thermospheric body force at $z\sim180-190$ km.

We now connect the above theoretical framework with our hypothesis of the source of the GWs observed by FPISR. We hypothesize that the tropospheric winds shown in Fig. 21 created mountain waves, which broke at $z\sim80$ km, creating large regions with rapid horizontal accelerations. Because these regions are coherent and last for several primary wave periods, they radiated high-frequency, large-amplitude GWs for several wave periods. Because of the coherency of the forcing, these secondary GWs appear as horizontally moving wave trains at higher altitudes (Vadas et al., 2003). However, because the duration of the horizontally accelerated region is limited to several primary wave periods, or 30 min to several hours, the duration of the wave train is also limited to several hours. This is why we likely see GW #1 last for only an hour, and GW #2 last for only 1.5 h. We postulate that each GW is from a different horizontal acceleration at $z\sim80$ km, that these different forcings were separated by an hour in time, and that these different forcings may have also been caused by wind flow over different mountain ridges/peaks. Note that the excited secondary GWs were excited propagating primarily N, NW, NE, S, SW, and SE (Vadas et al., 2003). For those SEward-propagating secondary GWs, many with larger λ_z propagated up to $z\sim180$ km (Vadas, 2007). At this altitude, most of the

Author's personal copy

excited spectrum with (1) $\lambda_H < 100$ km and (2) $\lambda_H > 100$ km and $\lambda_z \ll 100$ km, dissipated, similar to GWs from convective plumes. GWs #1 and 2 survived to much higher altitudes, however, because they had horizontal wavelengths of $\lambda_H > 100$ km and vertical wavelengths of $\lambda_z > 80$ km (Fritts and Vadas, 2008). Because these secondary GWs were moving SEward, the thermospheric body forces they created upon dissipating were SEward (VF2006). This is what is observed in the data. Additionally, the rapid acceleration that accompanies dissipation from a spectrum of GWs was also observed. These SEward accelerations were large at $t \sim 21.5$ UT in beams #3 and 6, and were large at $t \sim 23$ UT in beams #1, 2, and 4. Thus, the SEward neutral wind accelerations seen in the extracted winds indicate that thermospheric, neutral body forcing from dissipating GWs may have occurred. Although VF2006 estimated a full width half-max acceleration of $\simeq 0.1\,\mathrm{m/s^2}$ from a single convective plume, which is approximately the size of the accelerations observed here, the GWs here are secondary GWs excited from mountain wave breaking, not primary GWs excited from convection. A detailed study with (1) mountain wave generation and breaking, and (2) secondary GW excitation, propagation, and dissipation are needed to better compare this hypothesis with the data.

Finally, as mentioned previously, GW #2 disappeared from beams #8 and 10 at 23:00 UT. From Fig. 16, the neutral winds were rapidly accelerated over 25–30 min towards the SE from ~ -250 to ~ -100 m/s in beams #1, 2, and 4 at this time. These three beams are upstream of the propagation direction of GWs #1 and 2 from beams #8 and 10. We hypothesize that beams #1, 2 and 4 were at the edge of the body force, and that the main part of the body force was centered over beams #8 and 10. Since the winds in beams #1, 2 and 4 decreased to -100 m/s at $z \sim 190$ km (see Fig. 16), the winds in beams #8 and 10 would be even closer to zero. Since GW #2 dissipates at $z_{\mathrm{diss}} \sim 165$ km when the background winds are zero (square symbol in Fig. 2 in Vadas and Nicolls, 2008), we postulate that the reason GW #2 disappeared at 23:00 UT in beams #8 and 10 was because this GW encountered a very small thermospheric wind there because of the SEward thermospheric body force, and therefore dissipated at a much lower altitude than when the winds were ~ -250 m/s there (i.e., at $z < 190$ km). This would have prevented GW #2 from being observed in beams #8 and 10 for $t > 23.0$ UT, but it would not have prevented this GW from being observed N, NE, and NW of these beams, where the body force was less strong and therefore the NW thermospheric winds were not as weak.

6.3. Deceleration of the neutral wind from thermospheric dissipation

As mentioned previously, large SEward accelerations occurred at $t \sim 21.5$ UT in beams #3 and 6. After these accelerations ceased, NWward accelerations were observed in each of these beams. These NWward accelerations occurred over 50–80 min, and resulted in the winds relaxing back to their former large values of ~ -250 m/s towards the NW. This relaxation likely occurred because of kinematic viscosity. In this section, we investigate the time scales that viscosity acts to smooth out horizontal and vertical variations in the neutral winds created by thermospheric body forces.

Suppose a large, neutral, horizontal wind is created at $z \sim 190$ km from a thermospheric body force. Neglecting nonlinear effects and pressure divergences associated with vertical flows, the deceleration of this wind from kinematic viscosity is

$$\frac{\partial U}{\partial t} \simeq \nu \nabla U, \tag{55}$$

$$\frac{\partial V}{\partial t} \simeq \nu \nabla V, \tag{56}$$

where $\nabla \equiv \partial^2/\partial^2 x + \partial^2/\partial^2 y + \partial^2/\partial^2 z$. We assume that U and V vary in the horizontal and vertical directions as Gaussian functions for simplicity. We choose decaying solutions of the form

$$U = U_0 \exp(-t/\delta) \exp \times \left(-\frac{(x-x_0)^2}{2\sigma_x^2} - \frac{(y-y_0)^2}{2\sigma_y^2} - \frac{(z-z_0)^2}{2\sigma_z^2} \right), \tag{57}$$

$$V = V_0 \exp(-t/\delta) \exp \times \left(-\frac{(x-x_0)^2}{2\sigma_x^2} - \frac{(y-y_0)^2}{2\sigma_y^2} - \frac{(z-z_0)^2}{2\sigma_z^2} \right), \tag{58}$$

where U_0 and V_0 are the maximum values of U and V at $t = 0$, respectively. Note that the Gaussian distributions in x, y, and z capture the rapid and symmetric increase and decrease in the winds from a localized thermospheric body force (VF2006). Substituting Eqs. (57) and (58) into Eqs. (55) and (56), and evaluating the result at the location where the wind is the strongest (i.e., at (x_0, y_0, z_0)), the time scale for decay, δ, is

$$\delta \simeq \nu^{-1} \left(\frac{1}{\sigma_x^2} + \frac{1}{\sigma_y^2} + \frac{1}{\sigma_z^2} \right)^{-1}. \tag{59}$$

If the vertical variation of the created neutral wind is smaller than the horizontal variation, the decay time scale is

$$\delta \simeq \sigma_z^2/\nu. \tag{60}$$

If we assume a full vertical depth of the created wind of $\sim 50-60$ km, then $\sigma_z \simeq 55/4.5 \simeq 12$ km. Using the MSIS temperature profile assumed in Vadas and Nicolls (2008), $\nu \simeq 1.2 \times 10^5\,\mathrm{m^2/s}$ at $z \sim 190$ km. Then from Eq. (60), $\delta \sim 20$ min. Therefore, the created neutral wind at $z \simeq 190$ km decreases to 37%, 14%, and 5% of its initial value after ~ 20, ~ 40, and ~ 60 min, respectively, because of kinematic viscosity. Within an hour and a half of the horizontal wind being created at $z \sim 190$ km, it will have completely dissipated.

A further implication of this result is that neutral wind shears in the thermosphere (in excess of those created from tides), created from thermospheric body forces dissipate rapidly. For the zonal wind given by Eq. (57), the vertical wind shear is $(dU/dz)/U \sim -(z-z_0)/\sigma_z^2$, which is $|(dU/dz)/U| \sim 1/\sigma_z$ at $|z-z_0| \sim \sigma_z$. Setting $\sigma_z \sim 12$ km and $U \sim -200$ m/s at $z \sim 190$ km, the initial shear is $|dU_H/dz| \sim 17$ m/s/km, which is quite large. However, within ~ 20, ~ 40, and ~ 60 min, this shear is reduced to $|dU_H/dz| \sim 6$, 2, and 1 m/s/km, respectively, because of the overall decrease in the created neutral wind.

7. Conclusions

In this paper, we analyzed the temporal evolution of two GWs observed during a 4-h time period by PFISR on 13 December 2006 from 20:00 to 24:00 UT. In order to estimate the temporal variability of the extracted background winds which the GWs propagated through, we calculated the GW vertical wavelength along each maximum constant phase line. We then extracted the neutral, background, horizontal winds along the direction of GW propagation as a function of altitude every 10–12 min for all 10 beams by inputting λ_z and the measured GW parameters into an accurate, dissipative GW dispersion relation with MSIS temperatures. We find that the neutral, background wind along the NW–SE direction is to the NW and is composed of a slowly varying mean component with an average magnitude of ~ -150 m/s, plus a large-scale, slowly moving, upward-propagating wave with $\lambda_z \sim 80$ km and an observed period of $\sim 3-5$ h. We find that the mean wind increased towards the NW over the 4 h observation

Author's personal copy

window, and seemed to peak near 23–24 UT (at the end of the observation window). Because this time corresponds to 14–15 LST (a few hours after local noon), this "mean" wind was therefore likely due to the migrating diurnal tide, which is the dominant tide at $z \gtrsim 200$ km. While there is some uncertainty as to the absolute direction of the mean wind, it is likely in the NW direction from 20:00 to 24:00 UT. During geomagnetically quiet times, thermospheric winds above PF typically blow geographically NE at 00 UT, due to the in situ forced solar diurnal tide. With increasing magnetic activity, ion-drag forcing becomes a progressively larger contributor to the wind's momentum balance. This additional forcing by ion-drag tends to be directed NWward at 00 UT. Overall, the meridional component of the wind usually blows northward at 00 UT, whereas the zonal component is eastward on quiet days, but westward on active days (Mark Conde, personal communication).

Additionally, the $\sim 3-5$ h wave increased the NW wind at $z \sim 190$ km to ~ -250 m/s, and decreased the NW wind at $z \sim 230$ km to ~ -100 m/s, causing the background wind to decrease significantly with altitude over this altitude range. Note that the above mentioned method only determines the component of the background wind along the direction of GW propagation, which is NW–SE for these GWs. However, using the mean component of the anti-parallel ion velocity, Vadas and Nicolls (2008) found that the total wind vector was in a similar direction, $\sim 40^\circ$ counterclockwise from north.

The combined background wind caused the observed GWs to often have vertical propagation angles at $z \sim 180-200$ km, causing the GWs to be either evanescent or nearly evanescent at these altitudes. Because their amplitudes continued to increase up to $z \sim 110-225$ km, however, if the GWs were evanescent, then they must have tunneled through the vertical wind barrier. This was likely possible because λ_z was much larger than the vertical extent of the wind barrier.

We then analyzed the extracted winds for all 10 beams in the PFISR experiment at $z \sim 190$ km. We found that strong and rapid SEward accelerations in the winds occurred at these altitudes in the N, NE, and NW beams, with magnitudes as large as ~ 0.1 m/s^2. In comparison, the acceleration of GWs #1 or 2 at this altitude was much smaller $\sim (10\text{ m/s})/(20\text{ min}) \sim 0.01$ m/s^2. Additionally GWs #1 and 2 did not dissipate until $z \sim 220$ km, significantly above this altitude; therefore, it is highly unlikely that these SEward accelerations were due to GWs #1 and 2. These SEward accelerations created sudden changes in the neutral winds of $\sim 125-150$ m/s within 25–40 min. These accelerations appeared at similar times in adjacent beams, but did not occur in every beam, implying that there was a horizontal variation in the SEward accelerations on scales of order $\sim 50-100$ km. We also found that the winds relaxed back to their former values over time scales of 50–80 min, consistent with relaxation time scales from kinematic viscosity. We compared the observed thermospheric accelerations with previous work, and found that the time scales and peak altitudes of the accelerations are consistent with thermospheric body forcing which occurs when upward-propagating GWs from the atmosphere dissipate in the lower thermosphere. We hypothesized that these SEward accelerations are due to the dissipation of SEward-propagating GWs excited by the same mechanism which excited the observed GWs. We also hypothesized that these GWs are secondary GWs which were excited from mountain wave breaking near the mesopause $30-40^\circ$ to the NW of PFISR; this hypothesis is supported by the fact that, horizontally localized tropospheric winds were flowing northward over the Alaskan mountains $30-40^\circ$ to the NW of PFISR at the observation time, and that both observed GWs had ground-based periods of $\sim 20-24$ min, indicative of the frequencies that GWs excited near the mesopause must have in order to be observed by the PFISR radar beams in the F region. We do not know how common it is for GWs in the thermosphere to be secondary GWs from mountain wave breaking, because PFISR recently began operation, and only some analysis has been performed to date. Note that previous high-latitude measurements did not have the unique capability to measure the GW horizontal wavelengths and direction of propagation (e.g., Pinger, 1979), and therefore could not have determined the source of these waves. However, wintertime conditions over Alaska frequently exhibit large winds over the mountains and favorable stratospheric and mesospheric winds, which allow mountain waves (which have zero-phase speeds) to propagate to the upper mesosphere where they can break and cause the excitation of secondary GWs. Therefore, we believe that this source of GWs may be common in the wintertime at high latitudes. Further study with other wintertime PFISR data sets which contain medium-scale TIDs (MSTIDs) are needed to verify this conjecture.

Finally, we inputted the calculated winds into a ray-trace model which incorporates thermospheric dissipation, and computed the horizontal and vertical velocity amplitudes of the GWs using a dissipative polarization relation. Using a simple, single-ion model, we estimated the plasma response. We found that the GW velocity amplitude along the direction of the magnetic field over PFISR agrees well with the measured LOS ion velocities, up to a constant multiplying factor which accounts for the unknown initial wave amplitude. The amplitudes peaked at $z \sim 220-250$ km for these GWs. We also found that the calculated electron density perturbations, $\delta N_e/\overline{N}_e$, agree qualitatively with the observed values. Here, $\delta N_e/\overline{N}_e$ peaks at $z \sim 180-190$ km, similar to the measured values, because $\delta N_e/\overline{N}_e$ is more sensitive to altitudes where the background electron density $\overline{N}_e$ varies rapidly with altitude, rather than where the GW amplitude is maximum.

Acknowledgments

SLV would like to thank Pete Stamus for Fig. 21 and for helpful analysis of the meteorological conditions in Alaska for this observation window. She would also like to thank Art Richmond, Dave Broutman, Mark Conde, and David C. Fritts for helpful discussions. We also thank the anonymous referees for helpful comments. This research was supported by NSF under Grant ATM-0537311. The data collection and analysis for PFISR was supported under NSF cooperative agreement ATM-0608577.

References

Cowling, D.H., Webb, H.D., Yeh, K.C., 1971. Group rays of internal gravity waves in a wind-stratified atmosphere. J. Geophys. Res. 76, 213–220.

DelGenio, A.D., Schubert, G., 1979. Gravity wave propagation in a diffusively separated atmosphere with height-dependent collision frequencies. J. Geophys. Res. 84, 4371–4378.

Djuth, F.T., Sulzer, M.P., Elder, J.H., Wickwar, V.B., 1997. High-resolution studies of atmosphere–ionosphere coupling at Arecibo Observatory, Puerto Rico. Radio Sci. 32, 2321–2344.

Earle, G.D., Mwene-Musumba, A., Vadas, S.L., 2008. Satellite-based measurements of gravity wave-induced mid-latitude plasma density perturbations. J. Geophys. Res. 113, A03303.

Evans, J.V., 1969. Theory and practice of ionosphere study by Thomson scatter radar. Proc. IEEE 57, 496–530.

Forbes, J.M., 1995. Tidal and planetary waves. In: Johnson, R.M., Killeen, T.L. (Eds.), The Upper Mesosphere and Lower Thermosphere: A Review of Experiment and Theory. American Geophysical Union, p. 356.

Francis, S.H., 1973. Acoustic-gravity modes and large-scale traveling ionospheric disturbances of a realistic dissipative atmosphere. J. Geophys. Res. 78, 2278–2301.

Fritts, D.C., Alexander, M.J., 2003. Gravity wave dynamics and effects in the middle atmosphere. Rev. Geophys. 41 (1), 1003.

Fritts, D.C., Vadas, S., 2008. Gravity wave penetration into the thermosphere: sensitivity to solar cycle variations and mean winds. Ann. Geophys. 26, 3841–3861.

Author's personal copy

Gossard, E.E., Hooke, W.H., 1975. Waves in the Atmosphere. Elsevier Scientific Publishing Co., Amsterdam, 456pp.
Hedin, A.E., 1991. Extension of the MSIS thermosphere model into the middle and lower atmosphere. J. Geophys. Res. 96, 1159–1172.
Hickey, M.P., Cole, K.D., 1987. A quartic dispersion equation for internal gravity waves in the thermosphere. J. Atmos. Terr. Phys. 49, 889–899.
Hickey, M.P., Cole, K.D., 1988. A numerical model for gravity wave dissipation in the thermosphere. J. Atmos. Terr. Phys. 50, 689–697.
Hines, C.O., 1960. Internal atmospheric gravity waves at ionospheric heights. Can. J. Phys. 38, 1441–1481.
Hines, C.O., 1968. An effect of molecular dissipation in upper atmospheric gravity waves. J. Atmos. Terr. Phys. 30, 845–849.
Hines, C.O., Hooke, W.H., 1970. Discussion of ionization effects on the propagation of acoustic-gravity waves in the ionosphere. J. Geophys. Res. 75, 2563–2568.
Hines, C.O., Hooke, W.H., 1972. Momentum deposition by atmospheric waves, and its effects on thermospheric circulation. Space Res. 12, 1157–1161.
Hocke, K., Schlegel, K., 1996. A review of atmospheric gravity waves and traveling ionospheric disturbances. Ann. Geophys. 14, 917–940.
Hocke, K., Schlegel, K., Kirchengast, G., 1996. Phase and amplitudes of TIDs in the high latitude *F*-region observed by EISCAT. Ann. Geophys. 58, 245–255.
Kirchengast, G., 1996. Elucidation of the physics of the gravity wave–TID relationship with the aid of theoretical simulations. J. Geophys. Res. 101 (A6), 13353–13368.
Kirchengast, G., Hocke, K., Schlegel, K., 1996. The gravity wave–TID relationship: insight via theoretical model—EISCAT data comparison. J. Atmos. Terr. Phys. 58, 233–243.
Klostermeyer, J., 1972. Numerical calculation of gravity wave propagation in a realistic thermosphere. J. Atmos. Terr. Phys. 34, 765–774.
Kundu, P., 1990. Fluid Dynamics. Academic Press, San Diego, 638pp.
Midgley, J.E., Liemohn, H.B., 1966. Gravity waves in a realistic atmosphere. J. Geophys. Res. 71, 3729–3748.
Nicolls, M.J., Heinselman, C.J., 2007. Three dimensional measurements of traveling ionospheric disturbances with the Poker Flat Advanced Modular Incoherent Scatter Radar. Geophys. Res. Lett. 34, L21104.
Pinger, W.H., 1979. Detection of traveling ionospheric disturbances with auroral zone incoherent scatter radar. Radio Sci. 14, 75–84.
Pitteway, M., Hines, C.O., 1963. The viscous damping of atmospheric gravity waves. Can. J. Phys. 41, 1935–1948.
Richmond, A.D., 1978. Gravity wave generation, propagation, and dissipation in the thermosphere. J. Geophys. Res. 83, 4131–4145.
Roble, R.G., 1995. Energetics of the mesosphere and thermosphere. In: Johnson, R.M., Killeen, T.L. (Eds.), The Upper Mesosphere and Lower Thermosphere: A Review of Experiment and Theory. American Geophysical Union, p. 356.
Schunk, R.W., Nagy, A.F., 2000. Ionospheres, Physics, Plasma Physics, and Chemistry. Cambridge University Press, Cambridge, 554pp.
Showen, R.L., 1979. The spectral measurement of plasma lines. Radio Sci. 3, 503–508.
Testud, J., Francois, P., 1971. Importance of diffusion processes in the interaction between neutral waves and ionization. J. Atmos. Terr. Phys. 33, 765–774.
Vadas, S.L., 2007. Horizontal and vertical propagation and dissipation of gravity waves in the thermosphere from lower atmospheric and thermospheric sources. J. Geophys. Res. 112, A06305.
Vadas, S.L., Fritts, D.C., 2005. Thermospheric responses to gravity waves: influences of increasing viscosity and thermal diffusivity. J. Geophys. Res. 110, D15103.
Vadas, S.L., Fritts, D.C., 2006. Influence of solar variability on gravity wave structure and dissipation in the thermosphere from tropospheric convection. J. Geophys. Res. 111, A10S12.
Vadas, S.L., Nicolls, M.J., 2008. Using PFISR measurements and gravity wave dissipative theory to determine the neutral, background thermospheric winds. Geophys. Res. Lett. 35, L02105.
Vadas, S.L., Fritts, D.C., Alexander, M., 2003. Mechanism for the generation of secondary waves in wave breaking regions. J. Atmos. Sci. 60, 194–214.
Volland, H., 1969. Full wave calculations of gravity wave propagation through the thermosphere. J. Geophys. Res. 74, 1786–1795.
Waldock, J.A., Jones, T.B., 1984. The effects of neutral winds on the propagation of medium-scale atmospheric gravity waves at mid-latitudes. J. Atmos. Terr. Phys. 46, 217–231.
Yanowitch, M., 1967. Effect of viscosity on gravity waves and the upper boundary condition. J. Fluid Mech. 29, 209–231.
Yeh, K.C., Liu, C.H., Youakim, M.Y., 1975. Attenuation of internal gravity waves in model atmospheres. Ann. Geophys. 31, 321–328.
Zhang, S.D., Yi, F., 2002. A numerical study of propagation characteristics of gravity wave packets propagating in a dissipative atmosphere. J. Geophys. Res. 107 (D14), 4222.